University of Bristol - Explore Bristol Research
General rights

Imaging covalent bond formation by H-atom scattering from Graphene

Hongyan Jiang[1,2†], Marvin Kammler[1,2†], Feizhi Ding[3], Yvonne Dorenkamp[1,2], Frederick R. Manby[4],

Alec. M. Wodtke[1,2,5*], Thomas F. Miller III[3*], Alexander Kandratsenka[2*], Oliver Bünermann[1,5*]

Affiliations: [1]Institute for Physical Chemistry, Georg-August University of Göttingen, Tammannstraße 6, 37077 Göttingen, Germany. [2]Department of Dynamics at Surfaces, Max Planck Institute for Biophysical Chemistry, Am Faßberg 11, 37077 Göttingen, Germany. [3]Division of Chemistry and Chemical Engineering, California Institute of Technology, Pasadena, CA 91125, USA. [4] School of Chemistry, University of Bristol, Bristol BS81TS, UK, [5]International Center for Advanced Studies of Energy Conversion, Georg-August University of Göttingen, Tammannstraße 6, 37077 Göttingen, Germany,

Author Contributions:

[†]These authors contributed equally to this project.

*All correspondence and requests for materials related to this study should be addressed to Oliver Bünermann (Email: Oliver.buenermann@chemie.uni-goettingen.de), Thomas F. Miller III (Email: tfm@caltech.edu), Alexander Kandratsenka (Email: akandra@gwdg.de) and Alec M. Wodtke (Email: alec.wodtke@mpibpc.mpg.de)
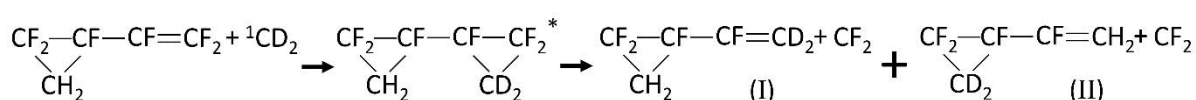
23 **Abstract**

24 Viewing the atomic scale motion and energy dissipation pathways involved in forming a co-

25 valent bond is a long standing challenge for chemistry. Here, we perform scattering experi-

26 ments of H atoms from graphene and observe a bimodal translational energy loss distribution.

27 Using accurate first-principles dynamics simulations we show that the quasi-elastic channel

28 involves scattering through the physisorption well where collision sites are near the centers of

29 the six-membered C-rings. The second channel results from transient C-H bond formation,

30 where H-atoms lose 1-2 eV of energy within a 10 *fs* interaction time. This remarkably rapid

31 form of intramolecular vibrational relaxation results from the C atom's re-hybridization dur-

32 ing bond formation and is responsible for an unexpectedly high sticking probability of H on

33 graphene.

34 **Introduction**

35 When a free-radical collides with an unsaturated molecule, electronic re-hybridization may

36 lead to formation of an addition complex with a great deal of energy initially localized in the

37 newly formed chemical bond. The addition complex is intrinsically unstable and may re-

38 dissociate; however, energy flow from the reactive site to the rest of the molecule can delay

39 this, allowing for isomerization, dissociation of other bonds or stabilizing collisions. Natural-

40 ly, there has been great interest to observe such energy flow in an addition complex, called

41 intramolecular vibrational redistribution (IVR). In the classic work of Rynbrandt and Rab-

42 inovitch, IVR within an addition complex was indirectly detected in the following reaction.

$$CF_2-CF-CF{=}CF_2 + {}^1CD_2 \;\rightarrow\; CF_2-CF-CF-CF_2{}^* \;\rightarrow\; CF_2-CF-CF{=}CD_2 + CF_2 \;+\; CF_2-CF-CF{=}CH_2 + CF_2$$

43
44

45 After $^1CD_2$ addition, energy is initially localized in only a part of the molecule (indicated by

46 a *). Before IVR is complete, one expects dissociation to produce excess (I), otherwise similar

47 amounts of (I) and (II) would form. By varying the pressure of an inert buffer gas and observ-

48 ing the branching between (I) and (II), the rate of energy flow could be determined. At the

49 highest buffer gas pressures used, CF_2 elimination occurred faster than ~1 *ps* after formation

50 of the addition complex. (At longer times the buffer gas quenched the energetic addition com-

51 plex.) Under these conditions, excess (I) resulted. When longer times for reaction were al-

52 lowed at lower buffer gas pressures, equal amounts of (I) and (II) were formed. This work

53 remains some of the strongest evidence that IVR proceeds in an addition complex within a

54 few *ps* (*1*).

55 Since then, IVR experiments with ultrafast PUMP-PROBE spectroscopy proliferated, where

56 short laser pulses were used to excite specific vibrational motions in stable molecules and

57 probe the rate of energy flow to other degrees of freedom (*2*). High-resolution spectroscopy

58 also helped identify the pathways of energy flow out of initially highly excited C-H stretching

59 motion (*3*). This large body of work (*4, 5*) confirmed that IVR proceeds on a *ps* time-scale

60 through a hierarchy of intramolecular processes involving gateway states (*6*) and bottlenecks

61 (*7*). Unfortunately, these spectroscopy experiments cannot tell us about the bond formation

62 process necessary to produce the addition complex.

63 Scattering experiments can directly probe collision complexes (*8*) and even reaction reso-

64 nances whose lifetimes are only a few *fs* (*9, 10*). In these studies, researchers produce a beam

65 of the incident free radicals with well-defined speed and direction. The speed and angular

66 distributions produced by the scattering are then analyzed with first principles simulations.

67 Scattering experiments and molecular dynamics simulations have also been used to develop

68 an atomic-level understanding of energy transfer, accommodation, and reactions during colli-

69 sions between gases and model organic surfaces (*11*). Scattering free radicals from surfaces

70 allows collision alignment and removes the influence of impact angular momentum, further

71 improving the fruitful interplay between experiment and theory (*12, 13*). To date, however,

72 scattering studies have never directly probed the direct interplay between chemical bond for-

73 mation and vibrational energy relaxation dynamics.

74 H atom chemisorption to graphene is relevant to hydrogen storage (*14*), the catalytic produc-

75 tion of molecular hydrogen in the interstellar medium (*15*) and two-dimensional semiconduc-

76 tor materials, because hydrogenation of graphene can induce a bandgap (*16*). For the purposes

77 of this study, H adsorption to graphene exhibits the most important features associated with

78 formation of an addition complex, namely re-hybridization during bond formation.

79 Figure 1 shows a 2D cut through a high dimensional potential energy surface (PES) devel-

80 oped in this work. Here, embedded mean-field theory (EMFT) electronic structure data (*17-*

81 *19*) is fitted with a reactive empirical bond order (REBO) function (*20*). See SI methods for

82 details of the PES. H approach to graphene leads to chemical bond formation coincident with

83 sp^2 to sp^3 re-hybridization of a C atom. This is reflected in the binding well being displaced

84 along the C_Z coordinate. The structural distortion induced by the electronic re-hybridization

85 gives rise to a barrier - if the H cannot overcome this barrier, the H atom will be reflected

86 (blue trajectory) without inducing re-hybridization. Alternatively, it may pass over the barrier,

87 induce re-hybridization and become trapped (gold trajectory) or scatter back to the gas phase

88 (black trajectory).

89 In this paper, we report H atom scattering experiments with graphene surfaces near zero cov-

90 erage, which removes well-known ambiguities (*21*) associated with the energy and coverage

91 dependence of C-H bond formation (*22*). H-atom scattering distributions resolve themselves

92 into a quasi-elastic and a strongly inelastic channel, determined by whether the barrier to

93 chemical bond formation is overcome. The observed inelastic energy transfer distributions

94 contain information about the rate of energy flow out of the newly formed C-H bond. By

95 comparing to molecular dynamics simulations carried out with a full-dimensional PES fit to

96 electronic structure data from a novel and accurate quantum embedding theory (*17*), we reveal

97 an energy loss mechanism able to remove electron volts of energy from the H atom within the

98 ~10 *fs* of a single-bounce collision. This surprisingly efficient energy flow out of a newly

99   formed chemical bond leads to unexpectedly high sticking probabilities of H on graphene. We

100   show that it is a result of electronic re-hybridization typical of bond formation leading to a

101   covalently bound addition complex.

102   **Results**

103   Figures 2A-C show experimental scattering distributions, $P(E_S; \vartheta_S)$, for collisions of H with

104   graphene grown on a Pt(111) substrate at an incidence energy of 1.92 eV. Pt was chosen as it

105   interacts weakly with graphene (*23*). Two scattering channels appear with narrow angular

106   distributions peaking close to the specular angle typical of direct "single-bounce" scattering.

107   The quasi-elastic ($E_S/E_I \sim 1$) "fast" channel dominates for large incidence angles, ϑ_I, and

108   gives way to a highly inelastic ($E_S/E_I \sim 0.5$) "slow" channel at small ϑ_I. First principles sim-

109   ulations - Fig.'s 2D-F - agree well with experiment and by analyzing trajectories - Fig. 2G -

110   we find that the slow channel results from trajectories forming a transient C-H bond, whereas

111   the fast channel arises from trajectories that failed to pass over the barrier to bond formation.

112   As ϑ_I decreases, H-atoms more easily cross the barrier, causing the slow channel to grow in

113   importance. This is further evidence for formation of a transient C-H bond that is most favor-

114   ably oriented at 90° to the graphene plane, formed efficiently with normal kinetic energy. We

115   also note that the total scattering signal drops in both experiment and simulation as ϑ_I de-

116   creases. This is partly a result of enhanced scattering out of the plane of detection in the slow

117   channel - see SI sec. S3, Fig. S7. It is also due to enhanced H atom sticking to the graphene

118   surface. Figure 3 shows the experimentally derived sticking probabilities, which increase with

119   the normal component of incidence energy. Here, we lowered E_I to 0.99 eV where sticking is

120   the fate of all H atoms that cross the barrier to C-H bond formation - See SI section S4, Fig.'s

121   S10&11. Under these conditions, only the quasi-elastic channel remains, for which out-of-

122   detection-plane scattering is more easily accounted for and measured survival probabilities

123   lead directly to reliable sticking probabilities. Theoretical simulations of sticking (black sym-

124   bols) are in excellent agreement with experiment - both show efficient sticking even at high

125   incidence energies and an adsorption threshold at $E_n \sim 0.4$ eV reflecting the influence of the

126   barrier to chemisorption.

127   There have been many theoretical predictions of the height of the barrier to C-H bond for-

128   mation on graphene (*24, 25*); up to now, no experimental validation has been possible. The

129   fact that our dynamical simulations agree well with experimental sticking probabilities argues

130   that the EMFT-REBO PES employed here is accurate. Fig. S2 shows the minimum energy

131   path for C-H bond formation comparing the EMFT-REBO PES to several other calculations

132   all for free standing graphene. We note that both the chemisorption well depth and the barrier

133   height found on the EMFT-REBO PES compare well with values found with CCSD(T) calcu-

134   lations of H addition to coronene (*24*).

135   The small deviations between experiment and simulation seen in Fig. 3 could be due to re-

136   maining errors in the PES, deficiencies in our treatment of the influence of Pt, which for ex-

137   ample does not properly treat C-Pt bond formation, or the classical approximation. Ring pol-

138   ymer molecular dynamics (*26, 27*) - open symbols in Fig. 3 - suggest that the net effect of

139   nuclear quantum effects are modest under the conditions studied here, in agreement with pre-

140   vious analysis (*28*). We also show calculated sticking probability curves with and without the

141   influence of the Pt substrate in Fig. S6 in SI sec. S2, suggesting also that the influence of Pt is

142   small.

143   **Discussion**

144   Figure 4 presents an analysis of trajectories to better understand the H atom translational en-

145   ergy loss and sticking mechanisms. Figure 4A shows that inelastic scattering is dominated by

146   ultrashort single-bounce events. The distribution of times spent within the chemisorption well

147   for the red and blue trajectories of Fig. 1G peaks at only ~10 fs - double bounce collisions can

148   also be seen clustered near 22 fs. Despite this, the H-atom energy loss is large. Fig. 4B pro-

149   vides additional insight; here the curves are averages over the subset of (60) trajectories for

150   which the H atom collides on top of a C atom. The kinetic energy that is lost from the incom-

151   ing H atom appears as increased kinetic and potential energy for graphene within 10-20 fs of

152   the initial collision; note that the kinetic energy of that C-atom directly involved in the colli-

153   sion hardly changes.

154   Instead, the neighbors of this C-atom absorb the energy released by transient C-H bond for-

155   mation. Fig. 4E shows the graphene structure, defined in terms of shells. Here, the 0th shell is

156   the C-atom struck by the H atom and the 1st shell reflects the three nearest neighbors. Re-

157   markably, Fig.'s 4C and D show that atoms in the 1st shell pick up kinetic energy first. The

158   creation of an electronically hybridized sp^3 C center during transient C-H bond formation ex-

159   erts strong in-plane forces between the 0th and 1st shell C-atoms. Subsequent to in-plane exci-

160   tation of 1st shell atoms, the H atom induces the 0th shell C atom to pucker out of the plane,

161   only fully experiencing the attractions of a sp^3-hybridized C-H bond once the puckering has

162   occurred and as the H atom is leaving. The SI contains an animation that shows the interaction

163   energy throughout a typical trajectory, revealing a bonding well is formed only at t>0, where

164   the H atom is recoiling back from the repulsive wall. After departure of the H atom, the de-

165   posited energy flows outward from the region of impact at close to the in-plane speed of

166   sound of graphene (*29*). See SI section S6, Fig. S16.

167   The large inelasticity seen in the slow channel is peculiar to a network of covalently bound

168   atoms, where C-H bond formation induces forces between multiple C-atoms by a disruption

169   of the delocalized covalent bonding network. This contrasts starkly with the interactions in the

170   fast, quasi-elastic channel - see SI section S7. Here, the H atom interacts with graphene

171   through van der Waals forces, which do not disturb the bonding between C-atoms of the gra-

172   phene. The most probable collision site giving rise to this kind of scattering is near the center

173   of the six-membered C-ring, where chemical bond formation is least likely. See Fig. S18.

174   Hence, the inelasticity in the fast channel follows the predictions of the hard cube model,

175   where the cube has the mass of 5-6 C atoms - see Fig. S17.

176   Next, we use our experimentally validated theoretical model to predict sticking under condi-

177   tions where it is difficult to measure. Theoretical simulations at E_I = 1.92 eV show large

178   sticking probabilities (Fig. 3 red symbols). Trapping is efficient, even for H atoms more than

179   2.5 eV above the potential energy minimum, more than 3x the binding well depth. Both the

180   experimental and simulated results presented in Fig. 3 contradict previous theoretical studies,

181   which predicted much smaller sticking probabilities (*28, 30-33*). See SI section S9 and Fig.

182   S19. This contradiction reflects deficiencies in previous models arising from reduced dimen-

183   sionality approximations as well as errors in the electronic energies produced by DFT at the

184   GGA level. We conclude that, due to the higher accuracy of the electronic energies made pos-

185   sible by the EMFT method and the ability to overcome reduced dimensionality approxima-

186   tions by use of a fitted REBO potential energy surfaces, that the results presented here are the

187   best present knowledge of the sticking probability of H on graphene grown on Pt.

188   This work also provides new insights into the fundamental steps of IVR in a newly formed

189   addition complex. For this analysis, we have also simulated IVR from a highly excited C-H

190   bond to the graphene substrate, for an initially puckered sp^3 hydrogenated graphene structure -

191   see SI section S9. These calculations show that when all energy is initially placed in H kinetic

192   or potential energy, relaxation takes place on two time-scales, with quasi-exponential life-

193   times of 0.5 and 3-4 ps, respectively. A vibrational relaxation time of 5 ps was previously

194   reported for H on graphene (*34, 35*). These processes reflect the coupling between different

195   vibrational degrees of freedom typical of an anharmonic interaction potential and the time-

196   scales seen here are similar to previous reports about IVR on stable molecules. A particularly

197   surprising aspect of this study is the discovery of a much faster energy loss mechanism requir-

198   ing only 10-20 *fs* to remove 1-2 eV of energy from the newly formed C-H bond. This process

199   proceeds on the time-scale of the C-network deformation induced by sp^2-sp^3 re-hybridization.

200   There is every reason to believe that this "re-hybridization IVR" plays an important role in the

201   recombination of many covalently bound free radicals forming addition complexes. In partic-

202   ular, we expect re-hybridization IVR to be a strong effect when the structural reorganization

203   associated with complex formation is large - implying the participation of many covalently

204   bound atoms - and when the frequencies associated with the distortion are high, making the

205   time-scale of energy uptake short. We note that in analogy to its important role in determining

206   the sticking probability of H to graphene, re-hybridization IVR is likely to be a determining

207   factor in calculating the collisional formation probability for addition complexes.

208   Supplementary Materials contains information on:
209   • **Methods**
210   • **The influence of the Pt substrate on the H atom scattering**
211   • **Out-of-detection-plane scattering**
212   • **H atom sticking probabilities at E_I = 0.99 eV**
213   • **A critical comparison of experiment and theory**
214   • **Sonic wave energy transport**
215   • **The hard cube model, the quasi-elastic channel and the site specificity of sticking**
216   • **Comparison to previous sticking probability work**
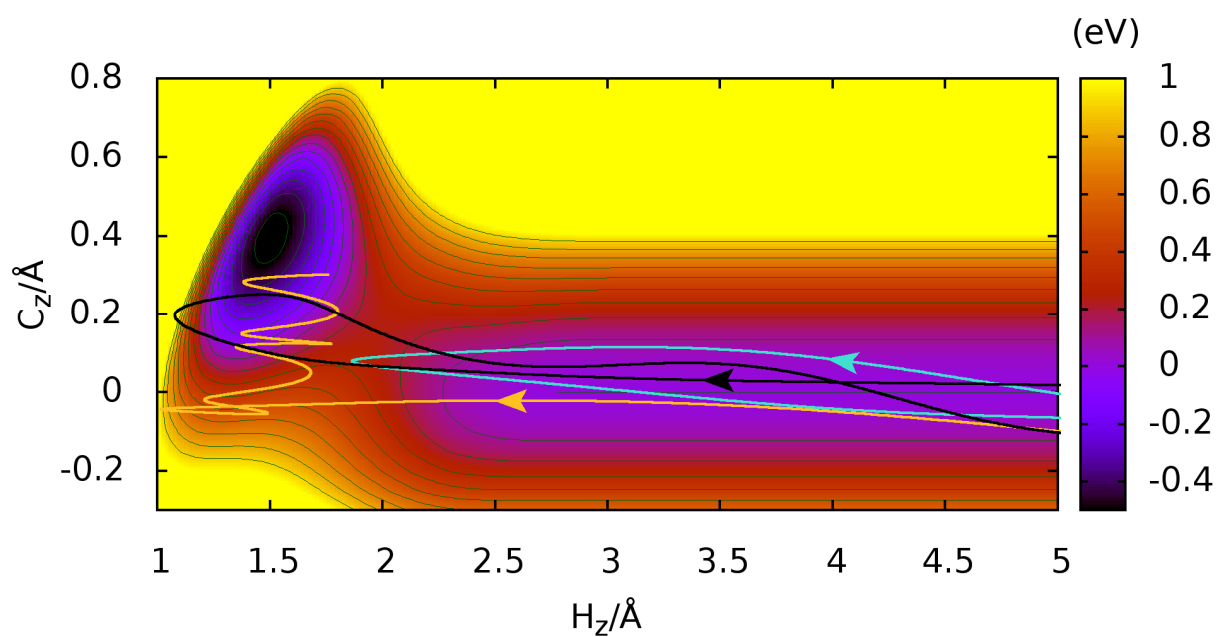217   • **Classical simulations of IVR lifetimes**
218

Figure 1: Re-hybridization in the formation of a C-H bond in collisions of an H atom at a graphene surface. H_Z and C_Z are the distances of the H and C atoms from the graphene plane. Three trajectories are shown for H atoms with 1.92 eV incidence energy.
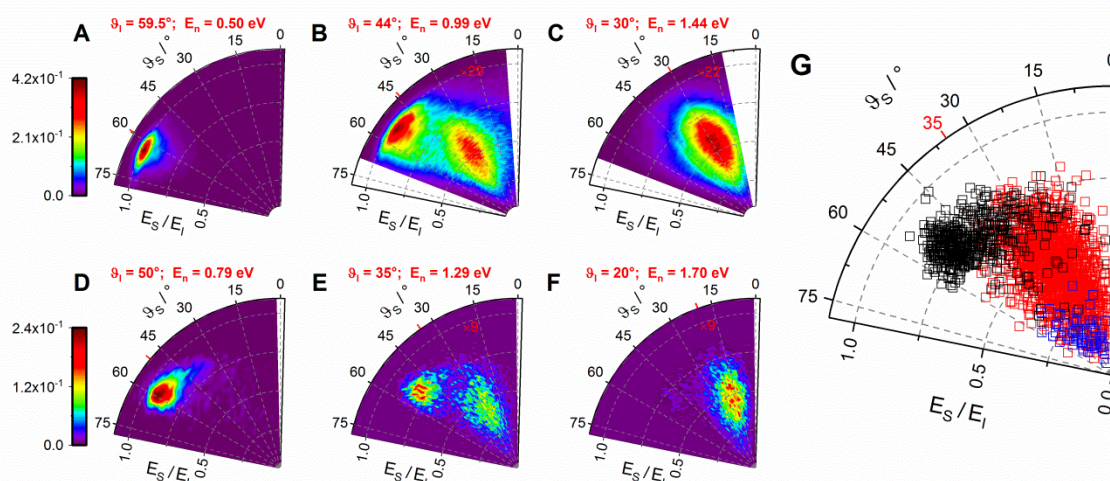
Fig. 2: Bimodal scattering distributions arising from H collisions with graphene. **A-C** show measured H atom scattering energy, E_S, and angular, ϑ_S, distributions with $E_I = 1.92$ eV. Results for three incidence angles, ϑ_I, are shown. Thus, the normal component of incidence energy, E_n, varies from 0.5 eV to 1.4 eV. $\vartheta_S = 0$ indicates the surface normal direction. Red ticks indicate the specular scattering angles. All observed scattering occurs within 2.8° of the plane defined by incident H atom beam and the surface normal. **D-F** show corresponding simulated scattering distributions, each shifted by ~10° in incidence angles. This shift is discussed in SI Section S5. Each distribution is multiplied by the indicated red number to use the same color bar. Each image represents one million trajectories. **G)** Analysis of theoretically calculated trajectories for $E_I = 1.92$ eV and $\vartheta_I = 35°$. Single bounce trajectories are shown as red and black. Those in black do not cross the barrier to chemical bond formation. A small number of multi-bounce collisions (blue) are also seen. The simulations include a modelled treatment of the graphene interactions with Pt. See SI section S2.
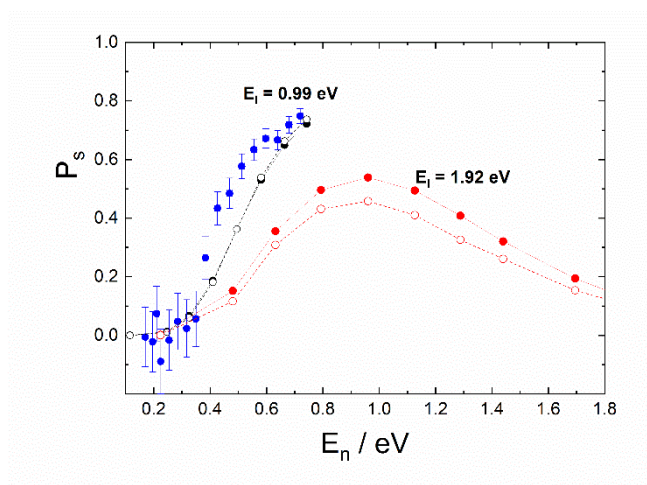
Fig. 3: H atom sticking probabilities at graphene. Experimentally derived (blue) and theoretically predicted (black) sticking probabilities for $E_I = 0.99$ eV plotted against the normal component incidence energy (E_n). Theoretically predicted sticking probabilities for $E_I = 1.92$ eV are shown in red. Theoretical simulations employed a full dimensional EMFT-REBO PES that includes the influence of the Pt substrate with classical molecular dynamics (solid symbols) or ring polymer molecular dynamics (open symbols).
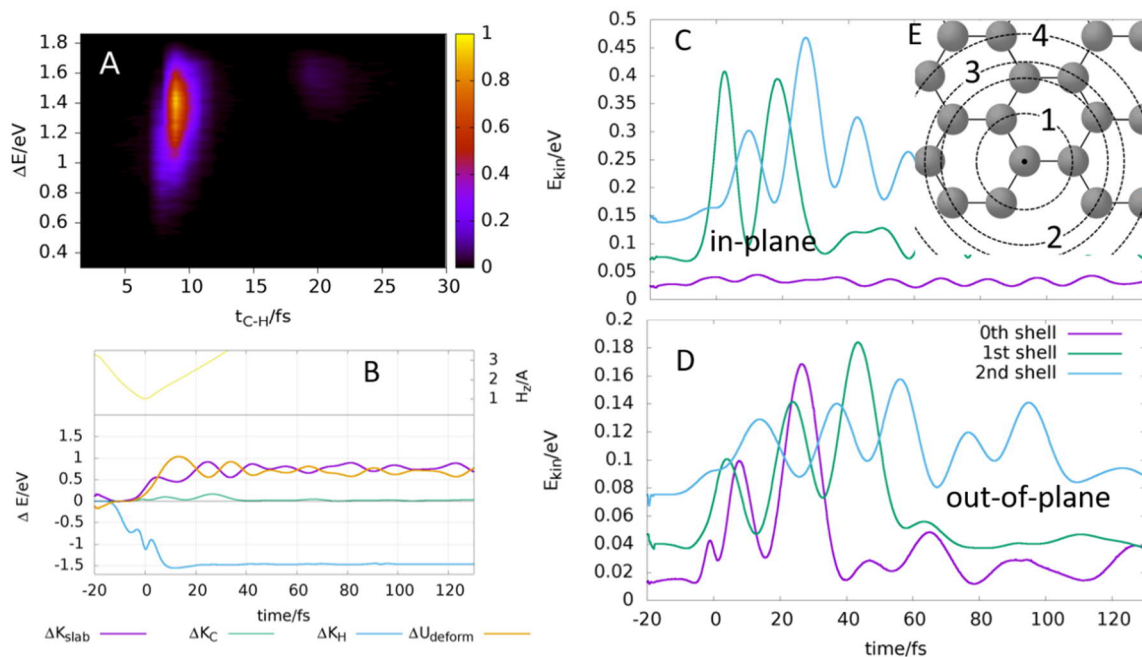
Fig. 4: The dynamical mechanism of energy transfer. **A)** the collision time correlation with H atom energy loss for trajectories that cross the barrier. The collision time is defined as the time spent with a C-H bond distance less than 1.4 Å. Panels **B**, **C & D**, show an average over 60 trajectories that collide on top of a C and pass over the barrier. A collision is labeled *on top* if at the point of closest approach one C-H distance is smaller than 1.15 Å and three and only three C-H distances are between 1.6 and 2 Å. t=0 is taken as the time of the H atom's closest approach. The incidence conditions are identical to those of Fig. 1G.The yellow curve in **B** shows the H distance to surface, H_Z; single bounce collisions dominate. Also shown are: the kinetic energy change of H atom (ΔK_H, blue); the kinetic energy change of all C atoms, (ΔK_{Slab}, purple); the kinetic energy of the C atom hit by the H atom (ΔK_C, green) and the graphene deformation energy, (ΔU_{deform}, gold). Panels **C and D** show the kinetic energy appearing in different C-shells. (The shell structure is shown in Panel **E**).

249

References

[1]   J. D. Rynbrandt, B. S. Rabinovitch, *Intramolecular energy relaxation - nonrandom decomposition of hexafluorobicyclopropyl*, J. Phys. Chem. **75**, 2164 (1971).

[2]   P. M. Felker, A. H. Zewail, *Direct picosecond time resolution of dissipative intramolecular vibrational-energy redistribution (IVR) in isolated molecules*, Chemical Physics Letters **108**, 303 (1984).

[3]   J. C. Keske, B. H. Pate, *Decoding the dynamical information embedded in highly mixed quantum states*, Annu. Rev. Phys. Chem. **51**, 323 (2000).

[4]   J. D. McDonald, *Creation and disposal of vibrational energy in polyatomic-molecules*, Annu. Rev. Phys. Chem. **30**, 29 (1979).

[5]   M. Gruebele, R. Bigwood, *Molecular vibrational energy flow: beyond the Golden Rule*, International Reviews in Physical Chemistry **17**, 91 (1998).

[6]   D. J. Nesbitt, R. W. Field, *Vibrational energy flow in highly excited molecules: Role of intramolecular vibrational redistribution*, J. Phys. Chem. **100**, 12735 (1996).

[7]   A. A. Stuchebrukhov, R. A. Marcus, *Theoretical-study of intramolecular vibrational-relaxation of acetylenic CH vibration for v = 1 and 2 in large polyatomic-molecules $(CX_3)_3YCCH$, where x = H or D and Y = C or SI*, Journal of Chemical Physics **98**, 6044 (1993).

[8]   J. M. Parson, Y. T. Lee, *Crossed molecular-beam study of $F+C_2H_4$, C_2D_4*, Journal of Chemical Physics **56**, 4658 (1972).

[9]   T. G. Yang, J. Chen, L. Huang, T. Wang, C. L. Xiao, Z. G. Sun, D. X. Dai, X. M. Yang, D. H. Zhang, *Extremely short-lived reaction resonances in Cl plus HD (v=1) -> DCl plus H due to chemical bond softening*, Science **347**, 60 (2015).

[10]   J. Srinivasan, T. C. Allison, D. W. Schwenke, D. G. Truhlar, *Transition state resonances in the reaction $Cl+H_2$ -> HCl+H*, Journal of Physical Chemistry A **103**, 1487 (1999).

[11]   J. W. Lu, B. S. Day, L. R. Fiegland, E. D. Davis, W. A. Alexander, D. Troya, J. R. Morris, *Interfacial energy exchange and reaction dynamics in collisions of gases on model organic surfaces*, Prog. Surf. Sci. **87**, 221 (2012).

[12]   O. Buenermann, H. Jiang, Y. Dorenkamp, A. Kandratsenka, S. M. Janke, D. J. Auerbach, A. M. Wodtke, *Electron-hole pair excitation determines the mechanism of hydrogen atom adsorption*, Science **350**, 1346 (2015).

[13]   S. M. Janke, D. J. Auerbach, A. M. Wodtke, A. Kandratsenka, *An accurate full-dimensional potential energy surface for H-Au(111): Importance of nonadiabatic electronic excitation in energy transfer and adsorption*, Journal of Chemical Physics **143**, 124708 (2015).

[14]   L. Schlapbach, A. Zuttel, *Hydrogen-storage materials for mobile applications*, Nature **414**, 353 (2001).

288 [15] L. Hornekaer, A. Baurichter, V. V. Petrunin, D. Field, A. C. Luntz, *Importance of*
289   *surface morphology in interstellar H_2 formation*, Science **302**, 1943 (2003).

290 [16] R. Balog, B. Jorgensen, L. Nilsson, M. Andersen, E. Rienks, M. Bianchi, M. Fanetti, E.
291   Laegsgaard, A. Baraldi, S. Lizzit, Z. Sljivancanin, F. Besenbacher, B. Hammer, T. G.
292   Pedersen, P. Hofmann, L. Hornekaer, *Bandgap opening in graphene induced by*
293   *patterned hydrogen adsorption*, Nat Mater **9**, 315 (2010).

294 [17] M. E. Fornace, J. Lee, K. Miyamoto, F. R. Manby, T. F. Miller, *Embedded Mean-*
295   *Field Theory*, Journal of Chemical Theory and Computation **11**, 568 (2015).

296 [18] F. Ding, F. R. Manby, T. F. Miller, *Embedded Mean-Field Theory with Block-*
297   *Orthogonalized Partitioning*, Journal of Chemical Theory and Computation **13**, 1605
298   (2017).

299 [19] F. Z. Ding, T. Tsuchiya, F. R. Manby, T. F. Miller, *Linear-Response Time-Dependent*
300   *Embedded Mean-Field Theory*, Journal of Chemical Theory and Computation **13**,
301   4216 (2017).

302 [20] D. W. Brenner, O. A. Shenderova, J. A. Harrison, S. J. Stuart, B. Ni, S. B. Sinnott, *A*
303   *second-generation reactive empirical bond order (REBO) potential energy expression*
304   *for hydrocarbons*, Journal of Physics-Condensed Matter **14**, 783 (2002).

305 [21] H. Kim, T. Balgar, E. Hasselbrink, *Is there sp^3-bound H on epitaxial graphene?*
306   *Evidence for adsorption on both sides of the sheet*, Chemical Physics Letters **546**, 12
307   (2012).

308 [22] L. Hornekaer, E. Rauls, W. Xu, Z. Sljivancanin, R. Otero, I. Stensgaard, E.
309   Laegsgaard, B. Hammer, F. Besenbacher, *Clustering of chemisorbed H(D) atoms on*
310   *the graphite (0001) surface due to preferential sticking*, Physical review letters **97**,
311   186102 (2006).

312 [23] I. Hamada, M. Otani, *Comparative van der Waals density-functional study of*
313   *graphene on metal surfaces*, Physical Review B **82**, 153412 (2010).

314 [24] Y. Wang, H. J. Qian, K. Morokuma, S. Irle, *Coupled cluster and density functional*
315   *theory calculations of atomic hydrogen chemisorption on pyrene and coronene as*
316   *model systems for graphene hydrogenation*, The journal of physical chemistry. A **116**,
317   7154 (2012).

318 [25] S. Casolo, O. M. Lovvik, R. Martinazzo, G. F. Tantardini, *Understanding adsorption*
319   *of hydrogen atoms on graphene*, Journal of Chemical Physics **130**, (2009).

320 [26] S. Habershon, D. E. Manolopoulos, T. E. Markland, T. F. Miller, III, in *Annual*
321   *Review of Physical Chemistry, Vol 64,* M. A. Johnson *et al.*, Eds. (2013), vol. 64, pp.
322   387-413.

323 [27] R. Welsch, K. Song, Q. Shi, S. C. Althorpe, T. F. Miller, III, *Non-equilibrium*
324   *dynamics from RPMD and CMD*, Journal of Chemical Physics **145**, 204118 (2016).

325 [28] M. Bonfanti, B. Jackson, K. H. Hughes, I. Burghardt, R. Martinazzo, *Quantum*
326   *dynamics of hydrogen atoms on graphene. II. Sticking*, J Chem Phys **143**, 124704
327   (2015).

328 [29] S. V. Dmitriev, J. A. Baimova, A. V. Savin, Y. S. Kivshar, *Ultimate strength, ripples,*
329   *sound velocities, and density of phonon states of strained graphene*, Comput. Mater.
330   Sci. **53**, 194 (2012).

331 [30] J. Kerwin, B. Jackson, *The sticking of H and D atoms on a graphite (0001) surface:*
332   *the effects of coverage and energy dissipation*, J Chem Phys **128**, 084702 (2008).

333 [31] S. Cazaux, S. Morisset, M. Spaans, A. Allouche, *When sticking influences H_2*
334   *formation*, Astronomy & Astrophysics **535**, A27 (2011).

335 [32] F. Karlicky, B. Lepetit, D. Lemoine, *Quantum modelling of hydrogen chemisorption*
336   *on graphene and graphite*, Journal of Chemical Physics **140**, 124702 (2014).

337 [33] S. Morisset, Y. Ferro, A. Allouche, *Study of the sticking of a hydrogen atom on a*
338   *graphite surface using a mixed classical-quantum dynamics method*, Journal of
339   Chemical Physics **133**, 10 (2010).

340 [34] S. Sakong, P. Kratzer, *Isotopic effect on the vibrational lifetime of the carbon-*
341   *deuterium stretch excitation on graphene*, Journal of Chemical Physics **135**, 7 (2011).

342 [35] S. Sakong, P. Kratzer, *Hydrogen vibrational modes on graphene and relaxation of the*
343   *C-H stretch excitation from first-principles calculations*, Journal of Chemical Physics
344   **133**, 8 (2010).

345 [36] O. Buenermann, H. Jiang, Y. Dorenkamp, D. J. Auerbach, A. M. Wodtke, *An*
346   *ultrahigh vacuum apparatus for H atom scattering from surfaces*, Review of Scientific
347   Instruments **89**, 094101 (2018).

348 [37] M. Svensson, S. Humbel, R. D. J. Froese, T. Matsubara, S. Sieber, K. Morokuma,
349   *ONIOM: A multilayered integrated MO+MM method for geometry optimizations and*
350   *single point energy predictions. A test for Diels-Alder reactions and Pt(P(t-*
351   *Bu)(3))(2)+H-2 oxidative addition*, J. Phys. Chem. **100**, 19357 (1996).

352 [38] D. W. Brenner, *The art and science of an analytic potential*, Physica Status Solidi B-
353   Basic Research **217**, 23 (2000).

354 [39] G. C. Abell, *Empirical chemical pseudopotential theory of molecular and metallic*
355   *bonding*, Physical Review B **31**, 6184 (1985).

356 [40] J. Tersoff, *New empirical-approach for the structure and energy of covalent systems*,
357   Physical Review B **37**, 6991 (1988).

358 [41] A. D. Becke, *Density-functional thermochemistry .3. The role of exact exchange*,
359   Journal of Chemical Physics **98**, 5648 (1993).

360 [42] C. T. Lee, W. T. Yang, R. G. Parr, *Development of the colle-salvetti correlation-*
361   *energy formula into a functional of the electron-density*, Physical Review B **37**, 785
362   (1988).

363 [43] S. H. Vosko, L. Wilk, M. Nusair, *Accurate spin-dependent electron liquid correlation*
364   *energies for local spin-density calculations - a critical analysis*, Canadian Journal of
365   Physics **58**, 1200 (1980).

366 [44] P. J. Stephens, F. J. Devlin, C. F. Chabalowski, M. J. Frisch, *Ab-initio calculation of*
367 *vibrational absorption and circular-dichroism spectra using density-functional force-*
368 *fields*, J. Phys. Chem. **98**, 11623 (1994).

369 [45] T. H. Dunning, *Gaussian-basis sets for use in correlated molecular calculations .1.*
370 *The atoms boron through neon and hydrogen*, Journal of Chemical Physics **90**, 1007
371 (1989).

372 [46] J. P. Perdew, K. Burke, M. Ernzerhof, *Generalized gradient approximation made*
373 *simple*, Physical review letters **77**, 3865 (1996).

374 [47] S. Grimme, *Semiempirical GGA-type density functional constructed with a long-range*
375 *dispersion correction*, Journal of Computational Chemistry **27**, 1787 (2006).

376 [48] P. Hohenberg, W. Kohn, *Inhomogeneous electron gas*, Physical Review B **136**, 864
377 (1964).

378 [49] W. J. Hehre, R. F. Stewart, J. A. Pople, *Self-consistent molecular-orbital methods .I.*
379 *Use of gaussian expansions of slater-type atomic orbitals*, Journal of Chemical
380 Physics **51**, 2657 (1969).

381 [50] F. R. Manby, T. F. Miller, P. Bygrave, F. Ding, T. Dresselhaus, F. A. Batista-Romero,
382 A. Buccheri, C. Bungey, S. J. R. Lee, R. Meli, K. Miyamoto, C. Steinmann, T.
383 Tsuchiya, M. Welborn, T. Wiles, Z. Williams, *entos: A quantum molecular simulation*
384 *package*, DOI: 10.26434/chemrxiv.7762646 (2019).

385 [51] G. Kresse, *Ab-initio molecular-dynamics for liquid-metals*, Journal of Non-Crystalline
386 Solids **193**, 222 (1995).

387 [52] G. Kresse, J. Hafner, *Ab-initio molecular-dynamics simulation of the liquid-metal*
388 *amorphous-semiconductor transition in germanium*, Physical Review B **49**, 14251
389 (1994).

390 [53] G. Kresse, J. Furthmuller, *Efficiency of ab-initio total energy calculations for metals*
391 *and semiconductors using a plane-wave basis set*, Comput. Mater. Sci. **6**, 15 (1996).

392 [54] G. Kresse, J. Furthmuller, *Efficient iterative schemes for ab initio total-energy*
393 *calculations using a plane-wave basis set*, Physical Review B **54**, 11169 (1996).

394 [55] P. E. Blöchl, *Projector augmented-wave method*, Physical Review B **50**, 17953 (1994).

395 [56] R. Polly, H. J. Werner, F. R. Manby, P. J. Knowles, *Fast Hartree-Fock theory using*
396 *local density fitting approximations*, Molecular Physics **102**, 2311 (2004).

397 [57] F. Weigend, *A fully direct RI-HF algorithm: Implementation, optimised auxiliary*
398 *basis sets, demonstration of accuracy and efficiency*, Physical Chemistry Chemical
399 Physics **4**, 4285 (2002).

400 [58] H. Shin, S. Kang, J. Koo, H. Lee, J. Kim, Y. Kwon, *Cohesion energetics of carbon*
401 *allotropes: Quantum Monte Carlo study*, Journal of Chemical Physics **140**, 114702
402 (2014).

403 [59] B. I. Dunlap, J. C. Boettger, *Local-density-functional study of the fullerenes, graphene*
404 *and graphite*, Journal of Physics B-Atomic Molecular and Optical Physics **29**, 4907
405 (1996).

406 [60] I. R. Craig, D. E. Manolopoulos, *Quantum statistics and classical mechanics: Real*
407 *time correlation functions from ring polymer molecular dynamics*, Journal of
408 Chemical Physics **121**, 3368 (2004).

409 [61] M. Ceriotti, M. Parrinello, T. E. Markland, D. E. Manolopoulos, *Efficient stochastic*
410 *thermostatting of path integral molecular dynamics*, Journal of Chemical Physics **133**,
411 124104 (2010).

412 [62] M. Andersen, L. Hornekaer, B. Hammer, *Graphene on metal surfaces and its*
413 *hydrogen adsorption: A meta-GGA functional study*, Physical Review B **86**, 085405
414 (2012).

415 [63] Y. J. Dorenkamp, Ph.D. Thesis, Georg-August Universtiy of Goettingen (2018).

416 [64] H. C. Andersen, *Molecular-dynamics simulations at constant pressure and-or*
417 *temperature*, Journal of Chemical Physics **72**, 2384 (1980).

418 [65] E. Bitzek, P. Koskinen, F. Gahler, M. Moseler, P. Gumbsch, *Structural relaxation*
419 *made simple*, Physical review letters **97**, 170201 (2006).

420 **References for SI**

421 36-65

422

Supplementary Material for

Imaging covalent bond formation by H-atom scattering from Graphene

Hongyan Jiang[1,2†], Marvin Kammler[1,2†], Feizhi Ding[3], Yvonne Dorenkamp[1,2], Frederick R. Manby[4], Alec. M. Wodtke[1,2,5*], Thomas F. Miller III[3*], Alexander Kandratsenka[2*], Oliver Bünermann[1,5*]

Affiliations: [1]Institute for Physical Chemistry, Georg-August University of Göttingen, Tammannstraße 6, 37077 Göttingen, Germany. [2]Department of Dynamics at Surfaces, Max Planck Institute for Biophysical Chemistry, Am Faßberg 11, 37077 Göttingen, Germany. [3]Division of Chemistry and Chemical Engineering, California Institute of Technology, Pasadena, CA 91125, USA. [4] School of Chemistry, University of Bristol, Bristol BS81TS, UK, [5]International Center for Advanced Studies of Energy Conversion, Georg-August University of Göttingen, Tammannstraße 6, 37077 Göttingen, Germany,

S1. Methods

Experimental procedures

The Pt(111) substrate was cleaned by several cycles of Ar^+ ion sputtering (30 mins) followed by annealing at 900°C (30 mins) and then flashing to 1000°C (2 mins). Surface cleanliness and structure were checked by Auger electron spectroscopy (AES) and low energy electron diffraction (LEED). The graphene sample was prepared by dosing ethylene on a clean Pt(111) substrate at 700 °C for 15 mins. The ethylene partial pressure was kept at 3×10^{-8} mbar during the dosing. The quality of the single layer graphene was confirmed by AES, LEED (Fig. S1) and by the comparison between scattering results from pristine Pt(111) surface and the graphene sample.
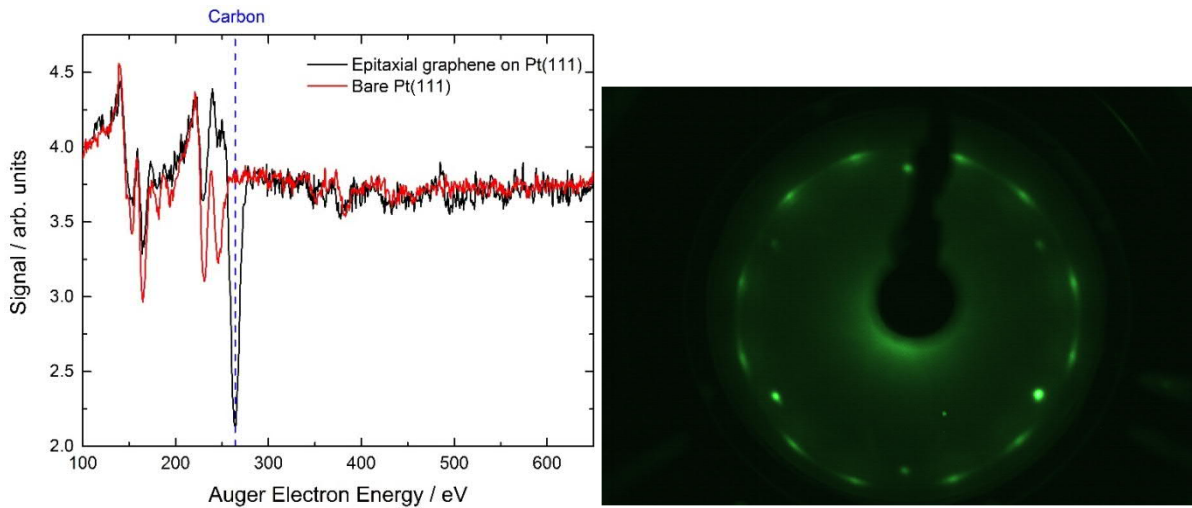
Figure S1: Characterization of graphene sample. (left panel) Auger spectrum of Pt(111) (red) and epitaxial graphene grown on Pt(111). The C Auger electron peak is marked by the blue dashed line. No other elements are detected, indicating the cleanliness of the surfaces. **(right panel) Low energy electron diffraction (LEED) spectrum of epitaxial graphene on Pt(111).** Electron incidence energy is 87 eV. The six circular diffraction spots at smaller polar diffraction angles are from Pt(111); three spots are dim and three bright. At slightly larger polar diffraction angles, twelve spots from graphene can be seen. Each of two orientational domains in the sample gives rise to six spots. The spots are broadened in the azimuthal direction, due to the weak interaction with Pt, which leads to a distribution of graphene Pt orientations with ~ 5˚ width.

The experimental apparatus has been described in detail in Ref. (*36*). Nearly mono-energetic hydrogen atom beams are generated by photolyzing a supersonic beam of hydrogen iodide with ArF or KrF excimer laser light. A small fraction of the atoms pass a skimmer, enter the first of two differential pumping chambers and pass into an ultrahigh vacuum chamber, where the graphene sample is held. The graphene is held on a 6-axis manipulator, allowing variation of the incidence angle, ϑ_I. The scattered H atoms are excited to a long lived Rydberg state by two spatially and temporally overlapped laser pulses passing parallel to the sample at a distance of 0.7 mm. The first laser pulse excites the 1s-2p transition at 121.57 nm and the second

466   excites the 2p-n=34 transition close to 365 nm. The neutral Rydberg atoms travel 250 mm

467   where they are field ionized and detected by an MCP. The arrival time is recorded using a

468   multi-channel scalar. The rotatable detector allows time-of-flight spectra to be recorded at

469   various scattering angles, ϑ_S. The H-atoms' incidence translational energy, E_I, can be con-

470   trolled by changing the photolysis wavelength. The normal component of the incidence trans-

471   lational energy can be varied by changing the incidence angle at a constant E_I.

472   ***Theoretical methods***

473   *General approach: Embedded mean-field theory*

474   Embedded mean-field theory (EMFT) (*17-19*) provides energies and forces from first-

475   principles for parameterization of the REBO potential. EMFT is an electronic structure em-

476   bedding approach that allows a subset of a system to be described using a relatively more ac-

477   curate but expensive mean-field theory (such as DFT with a hybrid functional and large basis

478   set), while the remainder of the system is described using a lower accuracy and cheaper mean-

479   field level (such as DFT with a LDA functional and a small basis set). In the EMFT method,

480   the subsystems are partitioned in terms of the atom-centered atomic orbital basis. Unlike the

481   ONIOM method (*37*), EMFT does not require specification of the number of electrons per

482   subsystem, nor does it require specification of the spin-state of the subsystem; only the total

483   number of electrons and the total spin-state of the system is specified. The method is accurate

484   and efficient over a wide range of systems and chemical applications, including those that

485   involve subsystem partitioning across conjugated bonding networks (*17-19*).

486   *General approach: Reactive empirical bond order potential*

487   The second generation reactive empirical bond order potential (REBO) was developed by

488   Brenner *et al.* (*20*) to describe various carbon modifications and hydrocarbons with an accu-

489   rate, flexible, transferable and computationally efficient analytic potential (*38*). It is based on

490   the ideas of Abell and Tersoff who assumed that the binding energy between two atoms can

491   be modeled by the sum of an attractive and a repulsive term (*39, 40*). The attractive term can

492   either be enhanced or weakened by a bond order factor. While attraction and repulsion is only

493   a function of the distance between two atoms, the bond order term also takes hybridization of

494   the carbon atoms into account. Information about an atoms hybridization is inferred from its

495   surroundings using Abell's argument that the bond order is proportional to the inverse square

496   root of the coordination number. REBO also includes the effects of radical species within a

497   molecular structure as well as rotation about dihedral angles for carbon–carbon double bonds.

498   The interaction range is limited by a cutoff function chosen in such that the nearest neighbors

499   are always accounted for while the second nearest neighbor are fully excluded. The strength

500   of the interaction is determined by multiple quadratic-, cubic- and higher-order, multi-

501   dimensional spline functions. The default parameter set for standard REBO was tuned to re-

502   produce the potential energy surfaces of solid carbon structures and small organic molecules.

503   Although REBO with its default parameter set has been successfully used for many hydrocar-

504   bon configurations, it does not give accurate results for H interactions with graphene. Conse-

505   quently, we used *ab initio* electronic structure data obtained from EMFT to train the parame-

506   ter set for accurate results in this system.

507   *Computational details. 1. Benchmarking the electronic structure methods.*

508   The current section compares the results of various electronic structure methods in describing

509   the binding-energy well depth and barrier height for an H atom interacting with graphene,

510   including the CCSD(T), DFT, EMFT, and EMFT-REBO methods. The CCSD(T) results were

511   previously reported (*24*). DFT calculations are performed with a hybrid functional using an

512   atom-centered Gaussian-type orbital (GTO) basis (B3LYP/cc-pVDZ) (*41-45*), as well as with

513   a GGA functional (PBE) (*46*) with Grimme D2 corrections (*47*) using a plane-wave basis with

514   a 400 eV cutoff and *k*-point sampling with a gamma-centered mesh of 8x8x1. EMFT results

515   are obtained with a B3LYP/cc-pVDZ description (*41-45*) for the atoms in the vicinity of the H

516   collision and with an LDA/STO-3G description (*43, 48, 49*) for the remaining atoms (see *Sec-*

517   *tion SI Computational Details 2* for details), and EMFT-REBO results are obtained using the

518   REBO method to fit the EMFT potential energy points (see *Section SI Computational Details*

519   *3* for details).

520   All EMFT and GTO-based DFT calculations reported in this study are performed using the

521   *entos* molecular simulation package (*50*). These calculations employ standard self-consistent

522   field (SCF) procedures, including use of superposition of the atomic densities (SAD) as the

523   initial guess, the direct inversion in the iterative subspace (DIIS) algorithm for SCF accelera-

524   tion, and a convergence threshold of 10^{-5} a.u. on the maximum value of the orbital gradient.

525   Plane-wave DFT calculations are performed using the VASP software package (*51-54*). For

526   the plane-wave calculations, spin polarization is included, and we employ the tetrahedron

527   method with Blöchl corrections (*55*) to treat partial occupancies with the default smearing

528   parameter of 0.2 eV. Interactions between the core and valence electrons are modeled by the

529   projector augmented wave approach (*55*). The relaxation of the electronic degrees of freedom

530   is stopped when the change in energy between iterations is smaller than 10^{-5} eV. In the calcu-

531   lations of the minimum energy pathway, convergence of the ionic relaxation loop is reached

532 when all forces are smaller than 10^{-3} eV/Å. The chemisorption well depth and barrier heights

533 are reported in Table S1, and the full MEPs are reported in Figure S2.

Table S1. Calculated chemisorption well depth and barrier height (in eV) for H atom on-top adsorption on graphene at various levels of theory.[a]

Graphene system	Method	Well depth (eV)	Barrier height (eV)
Coronene	CCSD(T)/cc-pVDZ[b]	-0.58	0.37
C$_{42}$H$_{16}$	B3LYP/cc-pVDZ	-0.80	0.27
	EMFT[c]	-0.59	0.28
Periodic (3 x 4 unit cell)	PBE/plane-wave	-0.84	0.14
Periodic (3 x 4 unit cell)	EMFT-REBO	-0.61	0.26

534 [a] The energy at dissociation limit is chosen as reference. Zero-point energy corrections are not includ-
535 ed. For finite-system calculations, basis set superposition errors are negligible and thus not included.
536 [b] Ref. (*24*).
537 [c] High-level : B3LYP/cc-pVDZ; low-level: LDA/STO-3G; Subsystem partitioning shown in Fig. S5.
538
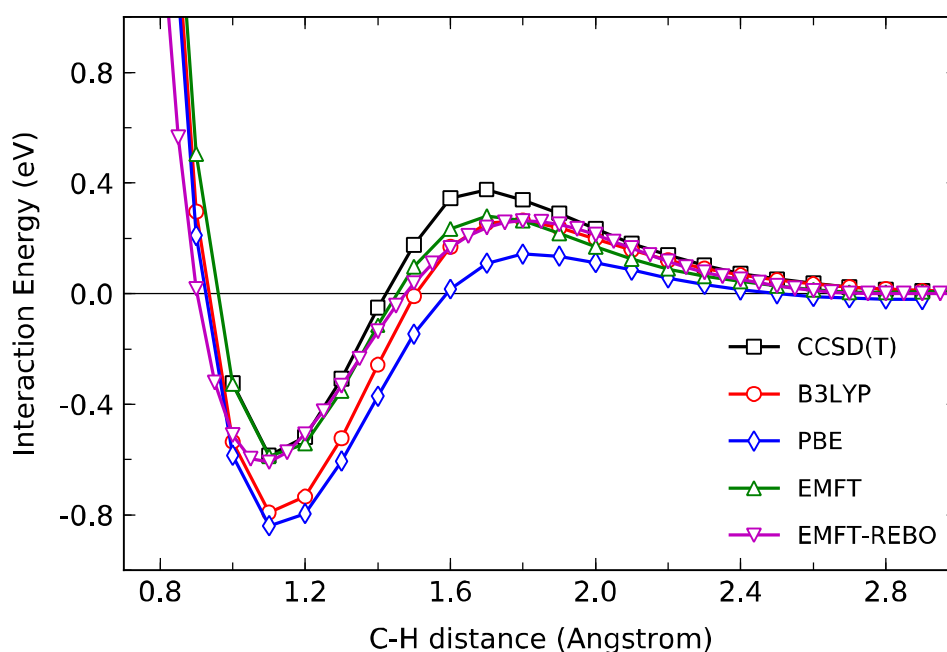
539

Figure S2. Calculated minimum energy path (MEP) for H atom on-top adsorption on free-standing graphene at various levels of theory. The levels of theory reported here are the same as in Table S1.

540

541 For the results in Table S1 and Fig. S2, the following system sizes were employed. The

542 CCSD(T) results (*24*) were obtained for an H atom interacting with the coronene graphene

543 flake, C$_{24}$H$_{12}$. The EMFT results and DFT results in the GTO basis were obtained for an H

544   atom interacting with a larger graphene flake, $C_{42}H_{16}$, and using 16 carbon atoms in the high-

545   level subsystem for the EMFT calculations (Fig. S2); additional benchmarking results with

546   larger graphene flakes are presented in *Section SI Computational Details 2*. The plane-wave

547   DFT and EMFT calculations were performed with periodic boundary conditions, using a sim-

548   ulation cell with 24 carbon atoms arranged such that the surface consists of 3 by 4 primitive

549   cells. A vacuum region of 13 Å above the graphene ensures that periodically stacked surfaces

550   do not interact with one another.

551   For the results in Table S1 and Fig. S2, the chemisorption well depth and barrier height are

552   examined in terms of the minimum energy path (MEP) along the on-top approach angle,

553   which corresponds to the H atom approaching the center carbon atom from the direction nor-

554   mal to the graphene surface. The reported DFT B3LYP/cc-pVDZ, PBE/plane-wave, and

555   EMFT-REBO energies are evaluated at geometries that were optimized at the same level of

556   theory; specifically, all degrees of freedom are relaxed at each fixed value for the C-H dis-

557   tance. The reported CCSD(T)/cc-pVDZ and EMFT energies are evaluated at the B3LYP/cc-

558   pVDZ-optimized geometries. The chemisorption well depth is computed as the electronic

559   energy difference between the minimum along this MEP and the system at infinite H-

560   graphene separation distance; the chemisorption barrier height is computed as the electronic

561   energy difference between the maximum along this MEP and the system at infinite H-

562   graphene separation distance.

563   In agreement with previous work (*24*), it is seen in Table S1 and Fig. S2 that the PBE/plane-

564   wave result underestimates the barrier height for the H-graphene interaction relative to

565   CCSD(T) by over a factor of two, whereas the B3LYP/cc-pVDZ description returns the calcu-

566   lated barrier height to with 0.1 eV of the CCSD(T) result. The EMFT description of the barri-

567   er height is essentially unchanged from that of the more costly B3LYP/cc-pVDZ calculations;

568   the well-depth for the EMFT description at these geometries is slightly lower than that of

569   B3LYP/cc-pVDZ, although it remains close to the CCSD(T)/cc-pVDZ description. Finally,

570   the EMFT-REBO calculations, which are directly parameterized on the basis of the EMFT

571   calculations, precisely reproduce both the EMFT barrier height and well depth. It is particu-

572   larly notable that while the EMFT results are obtained at B3LYP/cc-pVDZ-optimized geome-

573   tries while the EMFT-REBO results are obtained at EMFT-REBO-optimized geometries, the

574   resulting MEPs are essentially identical at all C-H separations; this indicates that the shape of

575   the EMFT-REBO, EMFT, and B3LYP/cc-pVDZ potential energy surfaces are all very simi-

576   lar, as is the goal of the methods. Taken together, these results indicate that the CCSD(T) re-

577 sults are reproduced well using EMFT for this system, and they demonstrate the fidelity with

578 which the EMFT-REBO results reproduce EMFT.

579 *Computational details. 2. EMFT calculation details and benchmarking.*

580 All EMFT calculations in the current study employ B3LYP-in-LDA embedding, with a high-

581 level subsystem described using DFT with the B3LYP hybrid functional (*41-44*) and the cc-

582 pVDZ basis set (*45*), while the surrounding environment is described using DFT with the

583 LDA functional (*43, 48*) and the minimal STO-3G basis set (*49*). The density-fitting approx-

584 imation with the cc-pVDZ/JKFIT (*56*) basis is employed for evaluation of the electron repul-

585 sion integrals (*57*). Both the atomic-orbital and density-fitting basis functions are implement-

586 ed as GTOs. All EMFT calculations are open-shell and employ spin-unrestricted orbitals.

587 Benchmark studies confirm that a graphene flake of $C_{42}H_{16}$ is sufficiently large to describe the

588 H-on-graphene interactions (Fig. S3) and confirm that a high-level subsystem comprised of

589 the colliding H atom and the 16 carbon atoms is necessary (Fig. S4). Based on these bench-

590 mark results, all EMFT results were performed for a system with a graphene flake of $C_{42}H_{16}$

591 using 16 carbon atoms in the high-level subsystem (Fig. S5), as well as including the scatter-

592 ing H in the high-level region. Using these parameters, the computational cost of the B3LYP-

593 in-LDA embedding description using EMFT is vastly reduced (over 11-fold) in comparison to

594 the computational cost of the full calculation performed at the B3LYP/cc-pVDZ level (Table
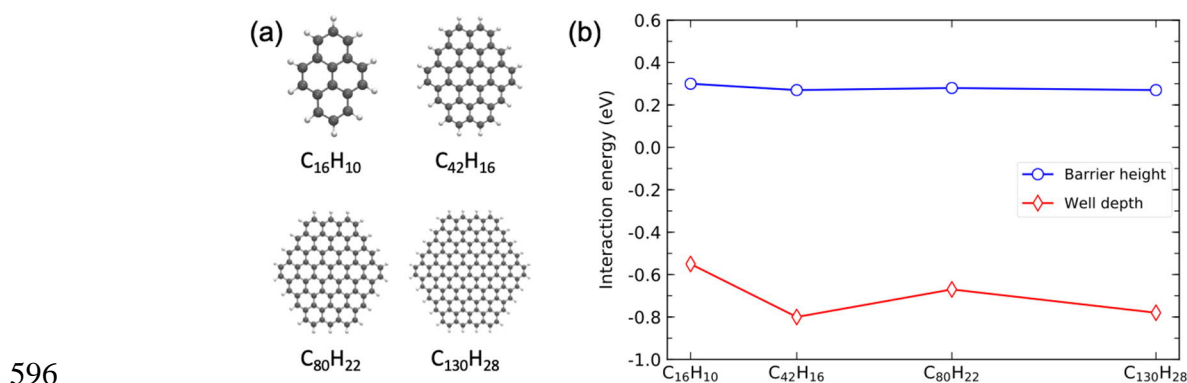
595 S2).

596

Figure S3. Graphene flake size dependence of chemisorption barrier height and well depth calculated at DFT B3LYP/cc-pVDZ level of theory. (a) graphene flakes studied in this work; (b) calculated chemisorption barrier height and well depth for different sizes of graphene flakes. All geometries are optimized at the DFT B3LYP/cc-pVDZ level of theory.
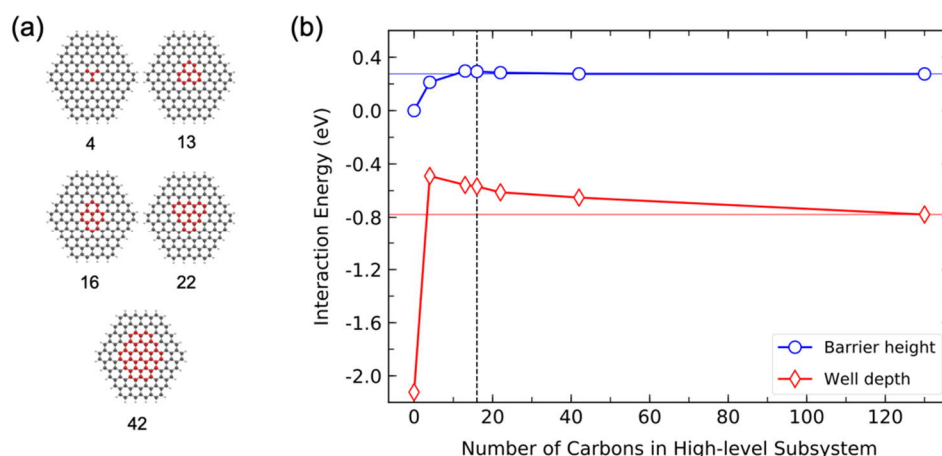
597

598

Figure S4. Accuracy of EMFT in chemisorption barrier height and well depth for the $C_{130}H_{28}$ graphene flake, relative to DFT B3LYP/cc-pVDZ level of theory. (a) Illustration of the different choices for the high-level subsystem that are considered; (b) EMFT barrier heights and well depths for different choices of the high-level subsystem. The blue horizontal line and red horizontal line correspond to DFT barrier height and well depth obtained at B3LYP/cc-pVDZ level of theory, respectively. The vertical dashed line corresponds to the high-level subsystem consisting of 16 carbon atoms. The relevant geometries are optimized at the B3LYP/cc-pVDZ level of theory.
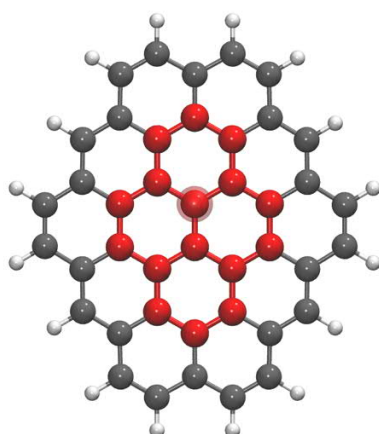
599

Figure S5. Partitioning of the $C_{42}H_{16}$ graphene flake for EMFT calculations. The atoms in red correspond to the high-level subsystem, and the remaining atoms correspond to the low-level subsystem. The carbon atom to which the H atom binds is highlighted.

Table S2. Timing comparison on single-point energy calculations using DFT and EMFT for H on $C_{42}H_{16}$ graphene flake.[a, b]

Method	Total time (seconds)	Relative speed-up
DFT[c]	521	1
EMFT	46	11.3

[a] Both calculations are performed using the same geometry optimized at the B3LYP/cc-pVDZ level of theory. For both calculations, convergence is achieved within 21 SCF iterations.
[b] Calculations are run on a NERSC Haswell computer with 32 cores and 128 GB DDR4 2133 MHz memory. Wall-clock times are reported.
[c] DFT calculation on full $C_{42}H_{16}$ flake at B3LYP/cc-pVDZ level of theory.

605   *Computational Details. 3. Fitting REBO using EMFT molecular dynamics simulations.*

606   *Ab initio* molecular dynamics (AIMD) simulations for the scattering experiment using EMFT

607   provide reference energies and forces for training of the REBO potential. The $C_{42}H_{16}$ flake is

608   used as the model system for graphene. We employ the EMFT subsystem partitioning with

609   the high-level subsystem comprised of the colliding H atom and the 16 carbon atoms (Fig.

610   S5). Initial conditions for AIMD trajectory calculations are set to mimic the experimental

611   conditions and to sample the configuration space needed for parameterization of the REBO

612   potential. These conditions include: (1) the initial coordinates and velocities of the graphene

613   atoms, which are sampled from a pre-equilibrated trajectory of the graphene at 300K using

614   Andersen thermostat; (2) the initial kinetic energy of the incident H atom is set to 1.92 eV;

615   (3) the target positions of the incident H atom are randomly distributed within the central unit

616   cell of the graphene flake; (4) the incident polar angles of the H atom range from 0° to 60°

617   with 10° spacing; (5) the incident azimuthal angles range from 0° to 180° with uniform ran-

618   dom distribution and (6) the initial H atom position is set 5 Å above the graphene surface.

619   In addition to the above trajectories, we also carry out simulations that start from the same

620   initial conditions except that the initial H atom is put 1.2 Å above the graphene surface, in

621   order to provide sufficient sampling for configurations that are near the chemisorption well

622   and barrier. A total number of ~ 400 EMFT trajectories were performed and 1600 data points

623   were used for the REBO parameterization.

624   The fit itself was performed with all three parts of the REBO PES, i.e., the C-C interaction,

625   the projectile-graphene interaction, and the interaction between the graphene flake and its

626   terminal H-atoms, being simultaneously fit. The parameters for the projectile H-atom and the

627   graphene terminal H-atoms were treated separately, to avoid having the large number of ter-

628   minal H-atoms unduly dominate the fitting; furthermore, the interaction between the graphene

629   flake and its terminal H-atoms can be disregarded when performing MD simulations with

630   periodic boundary conditions which eliminate the graphene terminal H-atoms. The fits were

631   done with the trust-region nonlinear least squares algorithm and convergence was achieved

632   typically after 12 local optimization steps. For each fit, the initial parameters were selected by

633   applying a Gaussian blur of 15% to each REBO parameter from the original publication, re-

634   sulting in an optimization in 27 dimensions.

635   The success of the re-parametrization is judged by several criteria. First, the root mean square

636   error (RMSE) must not differ much between the training and validation data; if the RMSE to

637   the training data was much lower than to the validation data, this would indicate overfitting.

638 The selected PES has an RMSE to the training data of 169 meV and the validation data can be
639 reproduced with an RMSE of 183 meV. Second, the carbon cohesive energy should not devi-
640 ate excessively from literature values; the employed PES predicts a cohesive energy of
641 12.3 eV for a carbon atom, while literature values range from 7-9 eV (*58, 59*). Third, cuts
642 through certain dimensions of the PES can be compared to reference calculations (see Fig.
643 S3); the re-parametrized REBO PES should be able to accurately predict energetic changes
644 during the adsorption process, i.e., barrier height, chemisorption well depth, and the correct
645 positions of both with respect to C-H distance from a top-site on the graphene surface.

646   *Computational Details 4: Ring-polymer molecular dynamics*
647 Ring-Polymer Molecular Dynamics (RPMD) is an approximate quantum dynamical method
648 that is based on Feynman's imaginary-time path integral formulation of statistical mechanics
649 (*26, 60*). RPMD enables quantum simulation via direct dynamics by providing a classical
650 molecular dynamics model for the real-time evolution of a quantum mechanical system. The
651 RPMD trajectories both preserve the exact quantum Boltzmann distribution and exhibit time-
652 reversal symmetry. The method has been demonstrated for the description of dynamics asso-
653 ciated with both thermal equilibrium initial conditions (*26*), as well as special cases of non-
654 equilibrium initial conditions (*27*). In the current study, we employ the "momentum impulse"
655 non-equilibrium conditions to describe graphene sheet at thermal equilibrium at 300 K but
656 with the colliding H atom initialized with a specified incident kinetic energy (*27*); in this pro-
657 tocol, the internal modes for the H-atom ring polymer are initially equilibrated at a tempera-
658 ture of 300 K, while the centroid mode of the H-atom ring polymer is initialized with the ve-
659 locity corresponding to the incident kinetic energy. The simulations were found to be suffi-
660 ciently converged using 12 ring-polymer beads. The thermalized initial distribution for the
661 graphene sheet was obtained using the path integral Langevin thermostat (*61*). In terms of the
662 position of the H atom, the RPMD scattering trajectories were initialized in the same way as
663 for the classical MD simulations, except with the position of the classical H atom replaced by
664 the centroid position of the ring polymer, and the scattering angle and final kinetic energy for
665 the RPMD trajectories were likewise determined from the centroid of the H-atom.

666 **S2. The influence of the Pt substrate on the H atom scattering**
667 Graphene primarily interacts with a Pt(111) surface through weak dispersion forces (*23*). The
668 EMFT-REBO approach just described was modified to include the effect of the Pt substrate
669 on the experimental observables. The substrate was modelled in the simulations using Len-
670 nard-Jones (LJ) potential interactions with each atom in the graphene layer. Specifically, car-

671 bon atoms in the graphene layer experience pair-wise interactions with a single layer of Pt
672 atoms that simulates the surface, via a potential of the form $V(r)=4\varepsilon*[(\sigma/r)^{12}-(\sigma/r)^{6}]$, where r is
673 the Pt-C distance, $\varepsilon = 250$ K and $\sigma = 2.95$ Å. This choice of parameters yields an interaction
674 energy between the Pt and graphene layers of 70 meV per C atom, which is consistent with
675 literature values (*62*).

676 Figure S6 shows the influence of this model of Pt-graphene interactions on the sticking prob-
677 abilities. For both incidence energies studied in this work, the sticking probability is slightly
678 enhanced at low E_I and slightly reduced at high E_I. For a finite surface temperature puckering
679 is enhanced compared to free-standing graphene by the asymmetry of the LJ potential. This
680 permits H atoms to more easily overcome the adsorption barrier. Indeed, when all degrees of
681 freedom are allowed to relax, the minimum energy path to adsorption takes place over a barri-
682 er that is 60 meV lower than on free-standing graphene. Meanwhile, the pre-puckering also
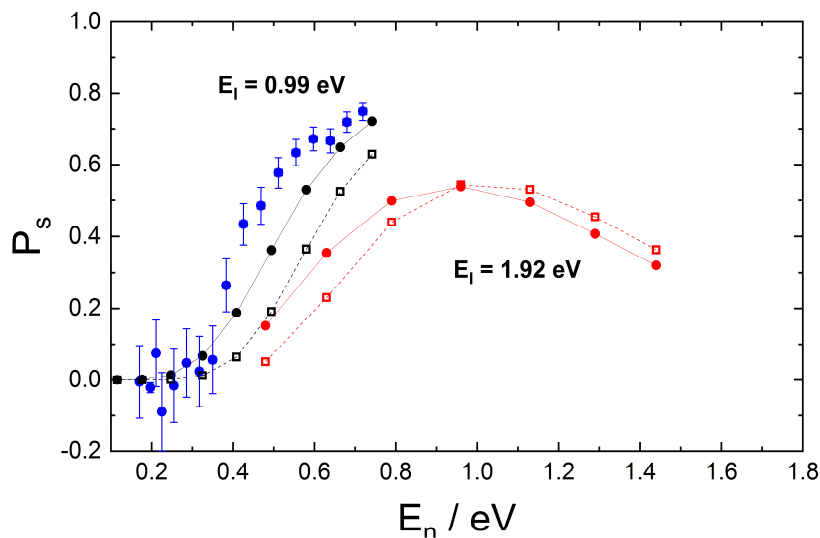683 results in a slightly smaller energy loss resulting in slightly less sticking at high E_n.

Figure S6: Influence of Pt substrate on sticking probability. Experimentally derived (blue) and theoretically predicted (black) sticking probabilities for $E_I = 0.99$ eV at various incidence angles in units of normal incidence energy (E_n). Results are for two cases: neglect of Pt (dashed lines, open symbols) versus inclusion of Pt by Lennard-Jones potential of van der Waals forces (solid lines, solid symbols). For $E_I = 1.92$ eV, the corresponding theoretical sticking probabilities are also presented (red), both neglecting (dashed lines, open symbols) and including (solid lines, solid symbols) the Pt substrate.

S3. Out-of-detection-plane scattering

685 The experimental data is only sensitive to H atom scattering that occurs in a detection plane
686 containing a vector along the initial H atom beam direction and a vector pointing from the H
687 atom impact point on the graphene sample to the detector. The normal vector of this detection

688 plane is parallel to the rotation axis of the detector. Figure S7 shows representations of scat-
689 tering simulations demonstrating the importance of scattering outside of the instrumental de-
690 tection plane. Here, the instrument detection plane corresponds to all values of ϑ where
691 $\varphi = 30°$.
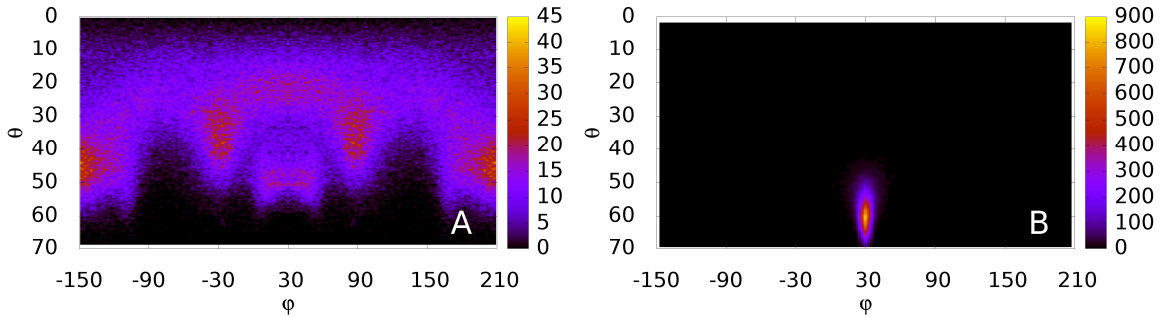
692
693 **Figure S7: Azimuthal scattering fluxes calculated from MD on the EMFT-REBO PES**
694 **assuming a single rotational orientation of the graphene crystal.** Here the initial condi-
695 tions are: E_I =1.92 eV, T_S =300K. **(A) transient chemical bond formation channel** exhibit-
696 ing scattering outside of the detection plane, ϑ_I =30°, φ_I =30°, and **(B) quasi-elastic chan-**
697 **nel** exhibiting scattering primarily within the detection plane ϑ_I =60°, φ_I =30°. φ_I =0° cor-
698 responds to H atom trajectories whose velocity vector projection onto the graphene plane
699 aligns with a C=C. φ_I = 30° corresponds to H atom trajectories whose velocity vector projec-
700 tion onto the graphene plane aligns perpendicular with a C=C.
701

702 For the slow channel where a transient chemical bond is formed, the MD calculations on the
703 EMFT-REBO PES show significant scattering probabilities out of the detection plane, when
704 the incidence angle ϑ_I =30° & φ_I = 30° (see Fig. S7-A). At this value of φ_I, the projection of
705 the H atom velocity vector onto the graphene plane is orthogonal to C=C bonds. The calcula-
706 tions predict a large amount of H atom flux out of the detection plane by this oriented colli-
707 sion. By contrast, the quasi-elastic channel shown in Figure S7-B, does not show this effect;
708 here, ϑ_I =60° & φ_I = 30° mainly gives rise to scattering within the detection plane. A similar
709 behavior can also be seen in theoretical predictions of the φ_I-dependence of the in-plane scat-
710 tering probability, Fig. S8. In-plane scattering is largest when the projection to the incident H
711 atom trajectory on the graphene plane aligns with a C=C and it is smallest, when the trajecto-
712 ry is aligned orthogonal to C=C bonds.

713
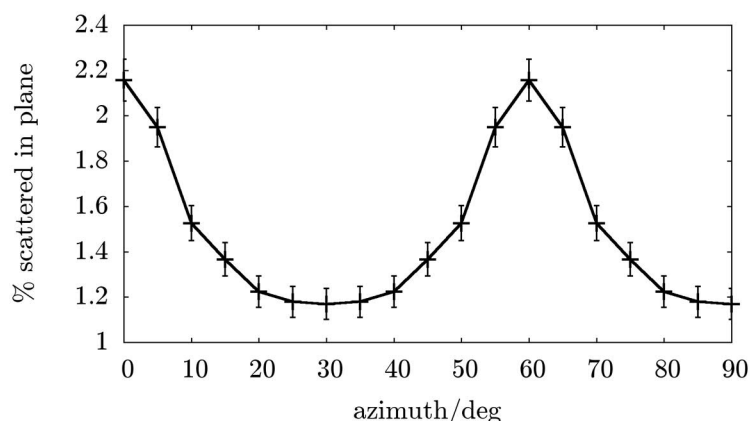
Figure S8: Azimuthal dependence of the in-plane signal. Crosses are calculated values and error bars indicate the 95% confidence interval. 0° and 60° are parallel to C=C bonds, and 30° and 90° are orthogonal to them. Incidence conditions are E_I=1.92 eV, ϑ_I =45°, where changes in the in-plane signal can be attributed to out-of-plane deflection during transient bond formation.

718

719 The graphene samples used in the experiments are not single crystals; they are composed of
720 two equally abundant orientational domains, one rotated by 27° with respect to the other.
721 Each domain has an orientational distribution of Gaussian with a width of ~5˚. The experi-
722 mental data was acquired with φ_I =13.5°, where the H atom velocity vector is oriented sym-
723 metrically with respect to these two orientational domains. To simulate experimental results,
724 both on sticking probabilities for E_I=1.92 eV presented in Fig. 3 and measured scattering
725 fluxes shown in Fig. 2, we have carried out calculations averaging over two rotational do-
726 mains oriented with φ_I =13.5°. Figure S9 shows how the out of plane structure in the scatter-
727 ing angular distributions is averaged out in scattering through the two domains.
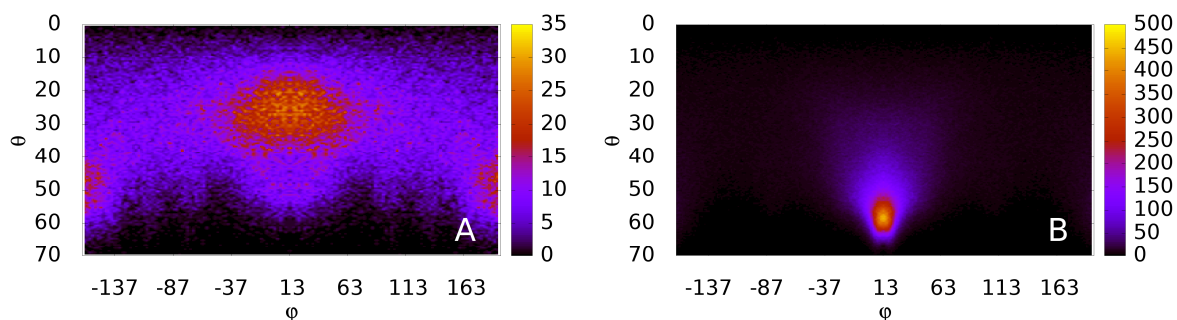
728
729 **Figure S9: Scattering fluxes calculated from MD on the EMFT-REBO PES averaging over two
730 orientational domains of the graphene crystal. (A) transient chemical bond formation channel**
731 present at ϑ_I =30° exhibiting scattering outside of the detection plane and **(B) quasi-elastic channel**
732 seen at ϑ_I =50° exhibiting scattering primarily within the detection plane. Here the initial conditions
733 are: E_I =1.92 eV, φ_I 13.5°, T_S =300K. The mechanical influence of the Pt-substrate was also taken
734 into account (see Sec. S2).

S4. H atom sticking probabilities at E_I = 0.99 eV

It is best to attempt an experimental determination of sticking probabilities where the scattering in the slow channel is unimportant, otherwise a careful and accurate accounting of out of detection plane scattering must be a part of the analysis. By lowering the incidence energy to E_i = 0.99 eV, where no slow channel is observed, we are able to observe the survival probability of the quasi-elastic channel as a function of normal incidence energy. Figure S10 shows a comparison of experiment and theory for E_i = 0.99 eV at three incidence angles. No slow channel is seen because the energy dissipation for low energy H atoms that cross the barrier to C-H bond formation is so efficient that re-crossing and escape back to the gas-phase does not occur. We can then use the experimental data to obtain the integrated scattered flux in the fast channel as a function of incidence angle, which is shown in Fig. S11. The survival probability increases as the normal component of incidence energy drops, reaching a plateau below E_n = 0.35 eV. Here we set the survival probability to 1 and use this to extract the sticking probability shown in Fig. 3 of the main text.
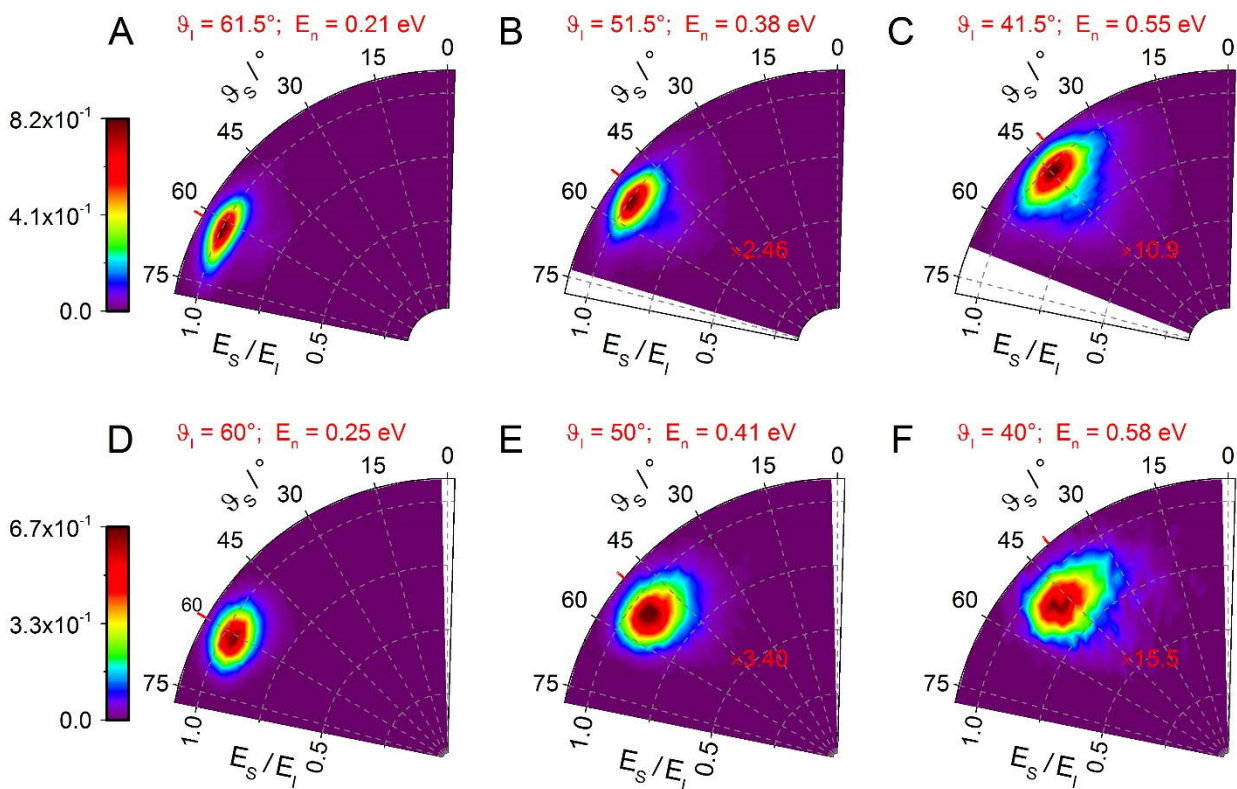
Figure S10: Scattering distributions of H collisions with graphene at E_I = 0.99 eV. A-C show measured H atom scattering energy, E_S, and angular, ϑ_S, distributions. Each distribution is multiplied by the indicated red number to use the same color bar. **D-F** show corresponding simulated scattering distributions. The incidence angles, ϑ_I and normal incidence energy, E_n, are also indicated ϑ_S =0 indicates the surface normal direction. Red ticks indicate the specular scattering angles. All observed scattering occurs within the plane defined by incident H atom beam and the surface normal.
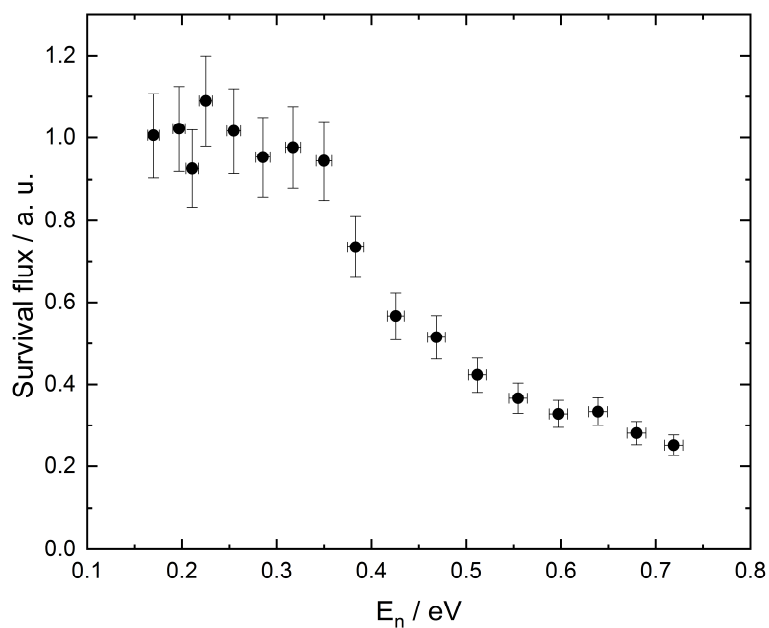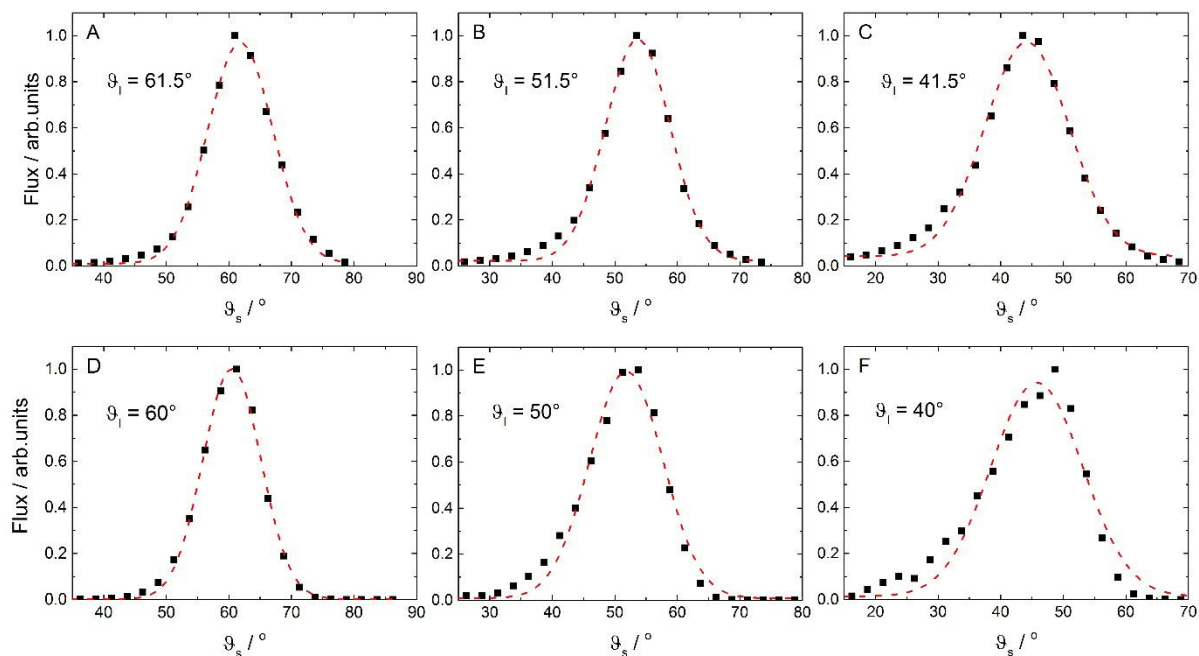
750

Figure S11: Experimentally derived survival flux using the data like that shown in Fig. S10.

751

752 This procedure requires an accounting of how the scattering angular distribution changes with

753 incidence angle. The angular distributions in the plane of detection are shown in Fig. S12A-C
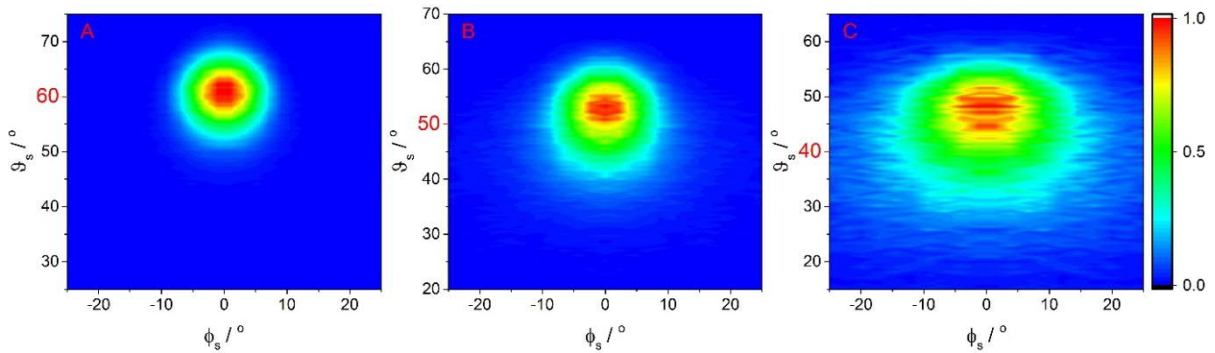
754 (experiment) and S12D-F (theory).

755

Figure S12: Experimental (A-C) and Theoretical (D-F) angular distribution of H atom scattering from graphene integrated over energy loss. The incidence conditions are the same with Fig. S10. Red dashed lines are Gaussian fits.

756

757   We integrate over the out-of-detection plane angles assuming cylindrical symmetry of the

758   angular distributions; Fig. S13 shows theoretical predictions that justify this assumption.

759

Figure S13: Calculated in-plane and out-of-plane angular distribution of H atom scattering from graphene integrated over energy loss. The incidence conditions are the same with Fig. S10 **D-F**. ϕ_s is the angle of the scattering direction relative to the plane defined by the incidence beam and surface normal. Scattering at $\phi_s = 0°$ corresponds to in-plane scattering.

760   **S5. A critical comparison of experiment and theory**

761   In Figure 2 of the main text, we uniformly shifted the simulated scattering flux distributions

762   by 10° in order to emphasize the similarities between the experiment and simulations. Figure

763   S14 shows the same comparison as in Fig. 2 without the 10° shift; here, incidence angles dif-

764   fer by less than 1°. The simulation agrees well with experiment at angles where only one

765   channel is present: $\vartheta_I = 60°$ shows only the fast channel and $\vartheta_I = 30°$ only slow channel. For

766   the intermediate angle, both channels are present in simulations and experiment, but the simu-

767   lations overestimate the fast component's relative contribution to the scattering signal.
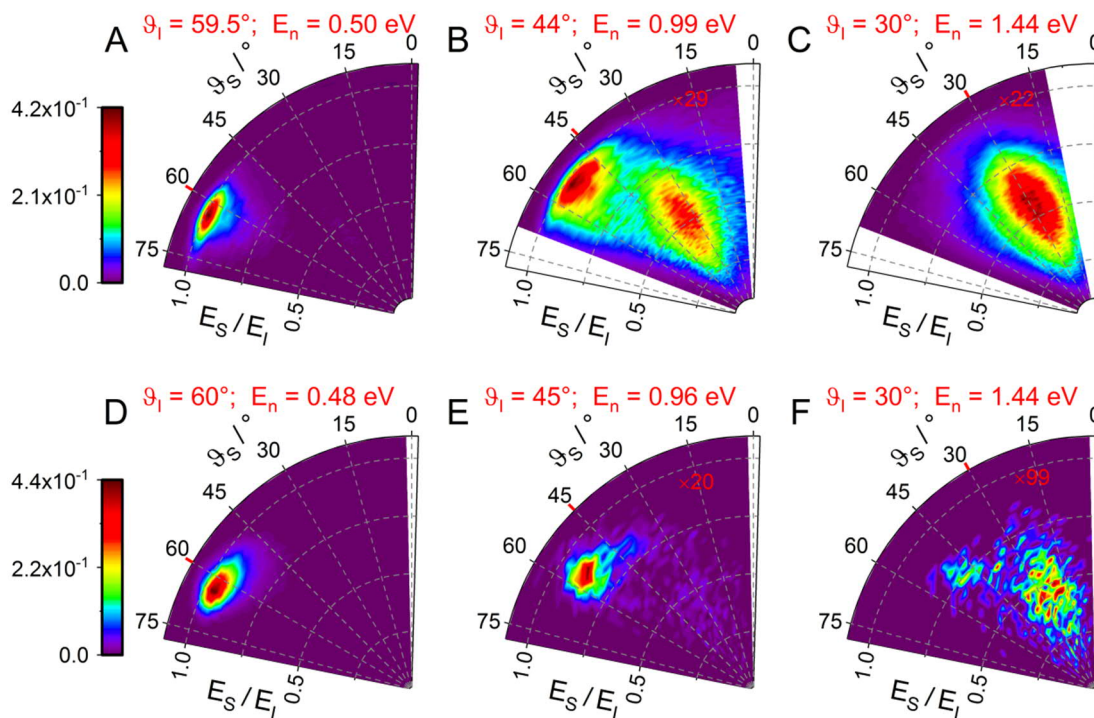
Figure S14: Scattering distributions of H collisions with graphene. **A-C** show measured H atom scattering energy, E_S, and angular, ϑ_S, distributions with $E_I = 1.92$ eV scattering. Each distribution is multiplied by the indicated red number to use the same color bar. **D-F** show corresponding simulated scattering distributions. The incidence angles ϑ_I and normal incidence energy, E_n, are indicated. $\vartheta_S = 0$ indicates the surface normal direction. Red ticks indicate the specular scattering angles. All observed scattering occurs within the plane defined by incident H atom beam and the surface normal.

769   These observations also appear in the angle-integrated energy loss distributions - Fig. S15.

770   Again, there is excellent agreement between the simulations and experiment at $\vartheta_I = 60°$ and

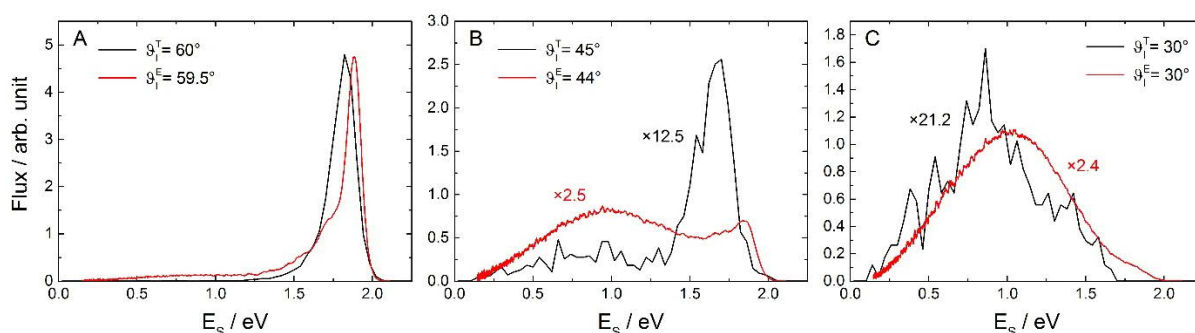771   30°, while the intermediate angle is biased towards the fast component.

Figure S15: Energy distribution for H atom scattering within the detection plane integrated over all polar scattering angles. The incidence conditions are the same with Fig. S14. ϑ_I^T and ϑ_I^E are incidence angles for theoretical simulation and experimental measurement, respectively. The multiplying factor indicates the signal drop.

773   The results in both Figs. S14 and S15 suggest that, despite broad agreement between the

774   simulations and experiment, the simulations predict a slightly higher energy threshold for C-H

775 bond formation than is seen in experiment. Evidence of this bias also appears in the predicted
776 sticking probabilities shown in Fig. 3, with the simulations requiring slightly more incidence
777 energy to overcome the barrier to C-H bond formation. These discrepancies could arise from
778 inaccuracies in the potential energy surface - possibly from the employed electronic structure
779 methods or the simplicity of the description of the Pt-graphene interactions. For example, the
780 increased degree of covalent bonding between graphene and Pt(111) that becomes possible
781 when a C-H bond is formed is not included in our treatment and will likely deepen the C-H
782 binding well and slightly lower the barrier as well.

783 Another possible source of discrepancy between experiment and simulation is the effect of
784 out-of-detection-plane scattering - see section S3. To the extent that the simulations do not
785 reproduce the scattering flux in both the fast and slow channels, the apparent branching be-
786 tween the two would differ from experiment. While the scattering effects reported here
787 emerge only from our theoretical analysis, the possible errors associated with azimuth-
788 specific scattering are likely to be small. We note that recent measurements on single crystal
789 graphene grown on Nickel show clearly that there is an influence of azimuthal incidence an-
790 gle on scattering probability (63). Moreover, the samples in the present work were polycrys-
791 talline; hence, they represent an average over two crystal orientations, an experimental condi-
792 tion that tends to wash out the influence of azimuthal specificity.

793 With these considerations in mind, we have allowed ourselves a global 10° shift in the polar
794 angle of Fig 2 to emphasize the broad similarities between the simulated and experimental
795 results. More important than the above described discrepancies, in our view, is that the ener-
796 gy loss predicted by the theory is nearly identical to that of experiment, as is clear from Figs.
797 S15 A&C. It is for this reason that excellent agreement between simulation and experiment is
798 obtained for the sticking probabilities in Fig. 3, where we duly note that no global polar angle
799 shift has been introduced.

800 **S6. Sonic wave energy transport**
801 Fig. S16 shows the time dependent displacement of carbon atoms involved most directly with
802 the H atom during the collision. As in Fig. 4, carbon atom shells are used to group neighbor-
803 ing atoms. When the H atom induced sp^2-sp^3 re-hybridization of the 0th shell C-atom occurs,
804 the length of its bonds to neighboring C atoms changes. As a consequence, the carbon atoms
805 in the 1st shell are initially pushed away from the center of impact. In turn, the second shell
806 carbon atoms are also deflected. This process continues and a wave propagates through the
807 graphene sheet. By monitoring the C-atom's displacements during simulation, we calculate

808   the speed of this wave to be ~18.6 km/s. This is similar to graphene's in-plane speed of sound

809   (22 km/s) determined by analysis of the LA phonon branch (*29*). This agreement with our

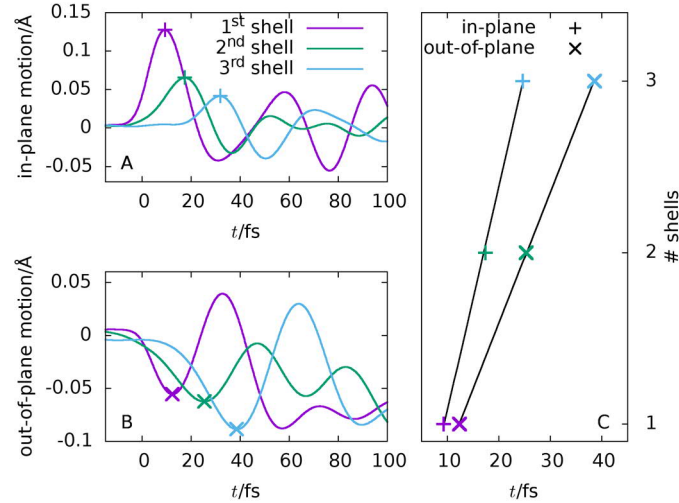810   simulations also argues for the overall accuracy of our EMFT-REBO PES.

Figure S16: Sonic wave energy dissipation. A) In-plane deflection of C-atoms in different shells from their respective equilibrium distance to the C-atom struck by the projectile. The maximum amplitudes are marked by pluses. Time zero is defined as the time of H atom closest approach. These results are the average of the 60 selected trajectories shown in Fig. 4B. **B)** Out-of-plane deflection of the carbon atoms in the same shells as in panel A. **C)** Points in time when the marked extrema in panel A and B are observed. From a least squares fit the speed of the outgoing waves is calculated to be 18.6 km/s in-plane and 10.9 km/s out-of-plane.

811   **S7. The hard cube model, the quasi-elastic channel and the site specificity of sticking**

812   Figure S17 shows a dynamical feature of the fast channel observed in this study that is mark-

813   edly different from the dynamics of the slow channel. Here, we compare predictions of the

814   hard cube model to experimental data for the fast channel. The hard cube model envisions the

815   H atom of mass m colliding with a flat surface of mass M at an incidence angle ϑ_I. The model

816   conserves momentum parallel to the surface allowing one to show that the energy loss ΔE, is

817   given by the following formula.

$$\Delta E = E_I - E_S = \left[\frac{4Mm}{(M+m)^2}\right]E_I cos^2\vartheta_I = \left[\frac{4Mm}{(M+m)^2}\right]E_n$$

818   Here M is the only adjustable parameter to fit the data (the red and black solid lines in Fig.

819   S17).
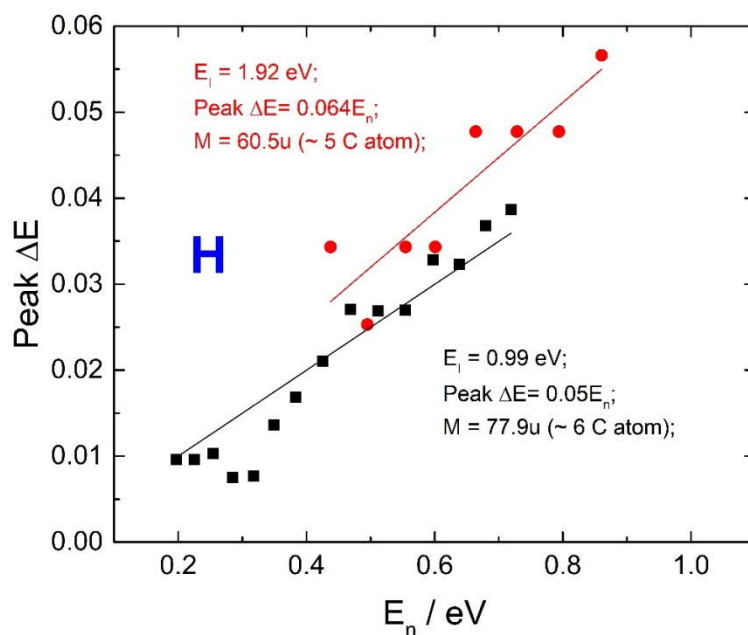
Figure S17: Most probable energy loss for the fast channel at various incidence angles in units of normal incidence energy E_n. Solid lines are fittings according to a hard cube model. Symbols are derived from experiment.

820

821

822 The effective mass of the hard cube, M, is close to the mass of 5-6 Carbon atoms. This sug-
823 gests that for the quasi-elastic channel, the H atom interacts with a six membered ring of C-
824 atoms.

825 The site-specific sticking probabilities, shown in Figure S18 for several incidence energies
826 help to explain this. At E_n =0.5 eV, sticking is more likely for collisions directly over C-
827 atoms, where the barrier is lowest. Conversely, quasi-elastic scattering occurs when H atoms
828 collide away from C-atoms, that is, for collisions over the center of the six membered rings.
829 As the incidence energy increases to E_n =1 eV, the sit-specific restrictions for sticking relax.
830 Conversely, the site specificity of the quasi-elastic channel increases. Here, the quasi-elastic
831 channel results from an impact precisely at the center of a six membered C-ring, where the H
832 atom is simply too far from any C atom to interact specifically with a single atom. Instead, the
833 picture emerges that the quasi-elastic channel resembles a collision with a rigid six membered
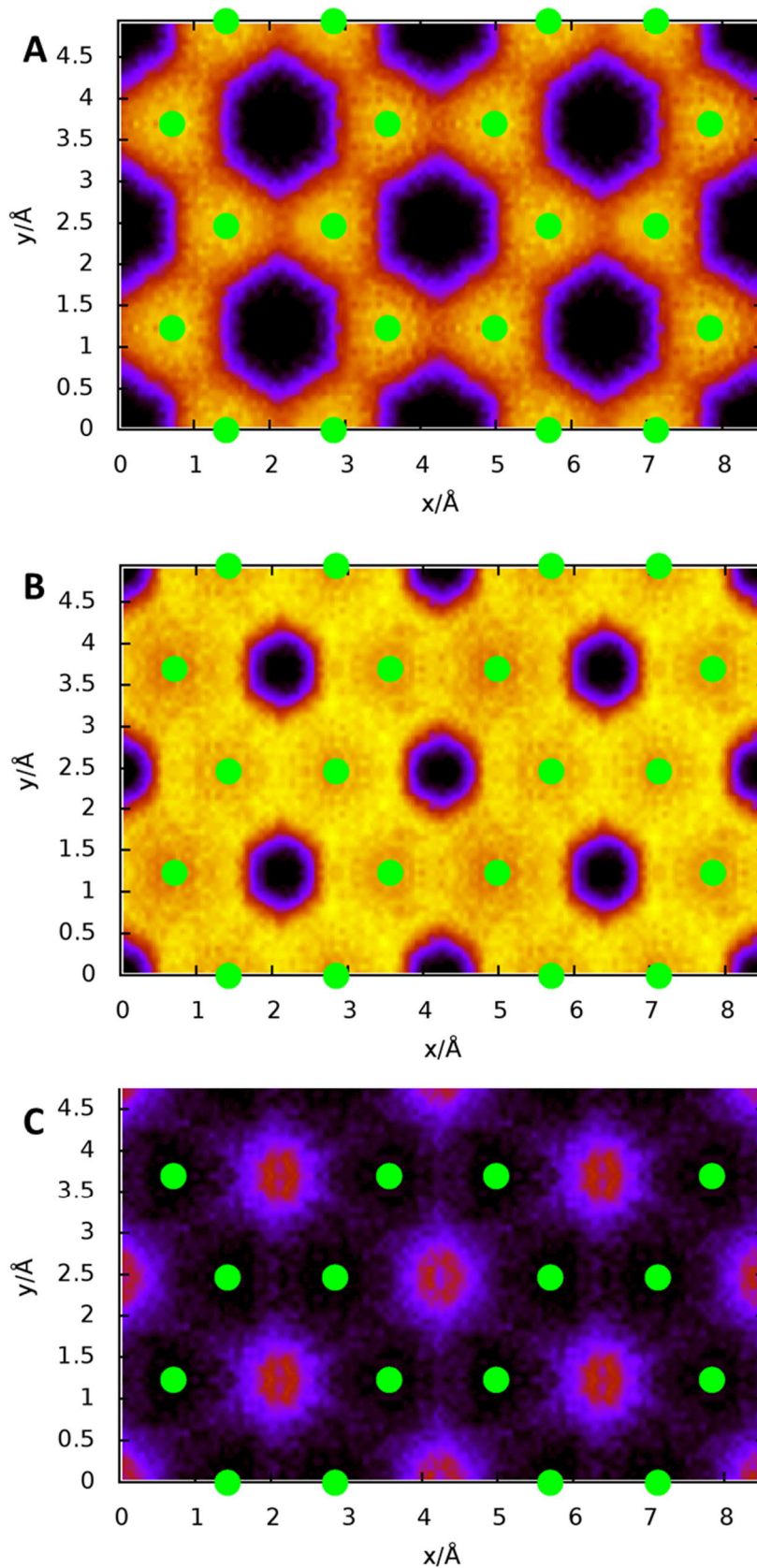834 C atom ring.

835

Figure S18: Heat Map representation of the site specific sticking of H atoms at graphene versus H atom incidence energy. A) $E_I = 0.5$ eV (near threshold). **B)** $E_I = 1.0$ eV (sticking probability maximum). **C)** $E_I = 2.0$ eV (incidence energy too high for efficient sticking). Incidence direction is along the surface normal. Green filled circles indicate position of C atoms. Increasing brightness of the color denotes increasing sticking probability.

836 At high incidence energies sticking and slow channel scattering dominate and compete with

837 one another. It is easy to understand that at E_I = 0.5 eV, only H-atoms that directly collide on

838 top of C atoms can stick. Top sites have the smallest adsorption barrier height and H atoms

839 that collide on other sites do not have enough energy to overcome the barrier. Furthermore,

840 the H atoms that pass over the barrier have low energies that dissipate rapidly into the gra-

841 phene. At high incidence energies, crossing the barrier is necessary but not sufficient for

842 sticking; dissipating the excess energy is also necessary. As can be seen in Fig. S18, directly

843 hitting the C atom no longer leads to the maximum probability for H atom sticking. In fact, at

844 E_I = 2.0 eV, sticking is only possible when the H atom avoids the top site. This allows some

845 of the normal incidence energy to be channeled into kinetic energy parallel to the surface, an

846 effect that suppresses re-crossing of the barrier.

847 **S8. Comparison to previous sticking probability work**

848 Figure S19 compares the sticking probabilities emerging from our experimentally validated

849 first principles calculations to those previously reported. The four previous reports all show

850 lower sticking probability than is found in this work. This deviation is larger at higher inci-
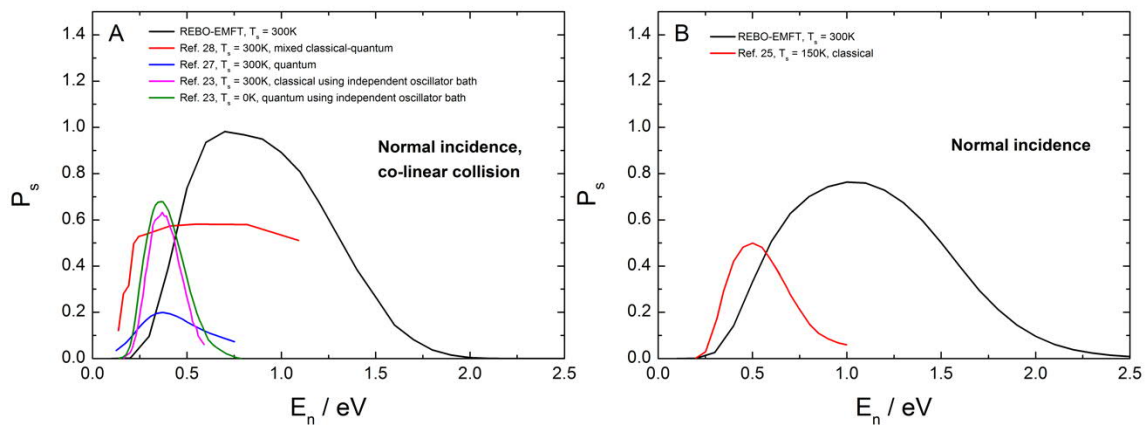
851 dence energies.

Figure S19: Comparison of theoretically predicted H sticking probabilities on graphene. A shows the H atom sticking probability for normal incidence and co-linear collision. T_s indicates the surface temperature in the simulation. E_n indicates the normal incidence energy (also the incidence energy). **B** shows the H atom sticking probability for normal incidence, and averaged over all impact parameters.

852 All of the methods (except that of Lemoine) appear to overestimate the sticking probability at

853 low energy and all methods underestimate the sticking probability at high energy. While the

854 previous studies all used different approaches, in light of the present work they all suffer from

855 a common flaw: they only consider the Z direction movement of the C atoms. Some also only

856 consider the Z motion of the H atom as well. In short, all of these approaches used reduced

857   dimensionality approximations that explicitly ignore concerted in-plane C-atom motion that
858   leads to the high H atom translational inelasticity seen in this work. In fact, even the most
859   recent reduced dimensionality theory agrees well with an impulsive collision model (*28*). This
860   differs starkly from the dynamics seen in our work. Furthermore, the use of DFT at the GGA
861   level to obtain input about the potential energy surface clearly results in a barrier to C-H bond
862   formation that is too low - this is likely the explanation for the overestimated sticking proba-
863   bility at low energy seen in several of the studies.

864   **S9. Classical simulations of IVR lifetimes**

865   Conventional IVR experiments utilize optical excitation of a molecule initially at its equilibri-
866   um configuration. For the H graphene system, we seek to simulate such an experiment by
867   initiating classical trajectories from an initial geometry that differs from the minimum energy
868   structure only by the displacement of the H atom. This initial state resembles one produced by
869   pumping a high overtone of the C-H stretch. To describe this, we set up the following simula-
870   tion.

871   H adsorbed on a graphene surface is equilibrated in phase space to 300 K using the Andersen
872   thermostat (*64*) in an NVT ensemble. Next, an NVE ensemble is simulated for 100 ps from
873   which a snapshot is taken every 100 fs. Then, in each of the 1000 snapshots, the H atom is
874   relaxed to the chemisorption well via the FIRE algorithm (*65*) while keeping all other degrees
875   of freedom fixed. This completes the stage of preparation of an ensemble of initial conditions
876   for the C atoms. Then for each initial total energy, we run 4500 NVE trajectories for 10 ps. A
877   trajectory is initialized by first selecting one of the geometry-optimized snapshots and displac-
878   ing the H-atom a certain distance either towards or away from the closest C-atom. This dis-
879   tance is randomly drawn from a uniform distribution ranging from -0.2 to 0.2 A. Next, the
880   change in potential energy is calculated and if it is lower than the total energy of the simula-
881   tion, the geometry is accepted and the remaining energy is provided as kinetic energy to the
882   H-atom, letting its initial velocity vector randomly either point towards the graphene sheet or
883   away from it. Finally, the trajectory is started in the NVE ensemble and the kinetic energy of
884   the H-atom is saved every 0.1 fs. To obtain the time-scales of IVR for the set of initial kinetic
885   energies, we average the kinetic energy of the H-atom in each time step over all trajectories in
886   which it remained attached to graphene. Dissociation was observed in less than 150 trajecto-
887   ries at any initial energy and the results are shown in Fig. S20A.
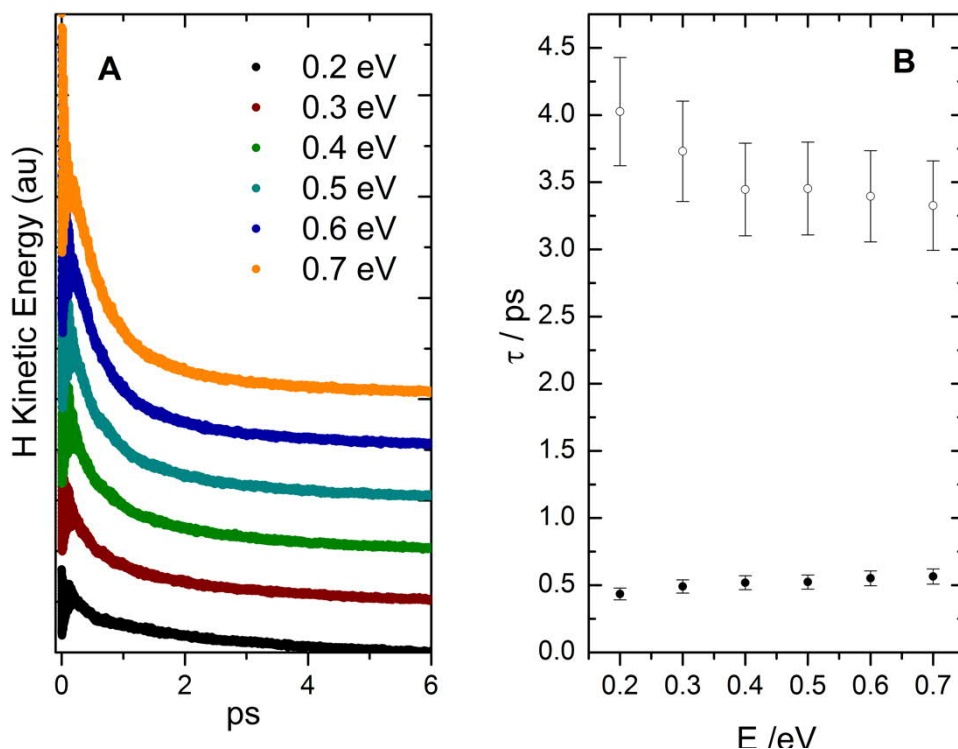
Figure S20: Classical Simulations of Intramolecular Vibrational Relaxation. A shows the H atom kinetic energy versus time at various initial energies. The plots are offset vertically from one another for clarity. Initially all energy is in either potential of kinetic energy of the H atom. The flow of H atom energy to the graphene slab takes place on the ps time-scale. The time dependence is best fit by a bi-exponential decay; the exponential lifetimes of the two process are shown in **B**. The error bars are estimated to be 10% of the lifetimes' values and they are mainly due to oscillations in the averaged data at early times.

888

889   The IVR follows a bi-exponential decay. It is comprised of a fast process that takes place in

890   approximately 0.5 ps and seems to decelerate toward higher energies and slow process taking

891   place on the order of several picoseconds- see Fig. S20B.

892